

Cosmological parameters from lensing power spectrum and bispectrum tomography

Masahiro Takada[★] and Bhuvnesh Jain[★]

Department of Physics and Astronomy, University of Pennsylvania, Philadelphia, PA 19104, USA

Accepted 2003 November 6. Received 2003 October 7

ABSTRACT

We examine how lensing tomography with the bispectrum and power spectrum can constrain cosmological parameters and the equation of state of dark energy. Our analysis uses the full information at the two- and three-point level from angular scales of a few degrees to 5 arcmin ($50 \leq l \leq 3000$), which will be probed by lensing surveys. We use all triangle configurations, cross-power spectra and bispectra constructed from up to three redshift bins with photometric redshifts, and all relevant covariances in our analysis.

We find that the parameter constraints from bispectrum tomography are comparable to those from power spectrum tomography. Combining the two improves parameter accuracies by a factor of 3 due to their complementarity. For the dark energy parametrization $w(a) = w_0 + w_a(1 - a)$, the marginalized errors from lensing alone are $\sigma(w_0) \sim 0.03 f_{\text{sky}}^{-1/2}$ and $\sigma(w_a) \sim 0.1 f_{\text{sky}}^{-1/2}$. We show that these constraints can be further improved when combined with measurements of the cosmic microwave background or Type Ia supernovae. The amplitude and shape of the mass power spectrum are also shown to be precisely constrained. We use hyperextended perturbation theory to compute the non-linear lensing bispectrum for dark energy models. Accurate model predictions of the bispectrum in the moderately non-linear regime, calibrated with numerical simulations, will be needed to realize the parameter accuracy we have estimated. Finally, we estimate how well the lensing bispectrum can constrain a model with primordial non-Gaussianity.

Key words: gravitational lensing – cosmology: theory – dark matter – large-scale structure of Universe.

1 INTRODUCTION

Various cosmological probes have given strong evidence that a dark energy component, such as the cosmological constant, constitutes approximately 70 per cent of the total energy density of the Universe. The most striking evidence comes from observations of supernovae in distant galaxies (Riess et al. 1998; Perlmutter et al. 1999a,b), mapping temperature anisotropies in the cosmic microwave background (CMB) sky (e.g. Spergel et al. 2003) and detections of the integrated Sachs–Wolfe effect via the cross-correlation between the CMB and the large-scale structure (Boughn & Crittenden 2003; Nolta et al. 2004; Scranton et al. 2004). If the dark energy is constant in time, its natural value is 50 to 120 orders of magnitude larger than the observed value (Weinberg 1989). A model that allows the dark energy to dynamically evolve could avoid this fine tuning problem (see Peebles & Ratra 2003 and Padmanabhan 2003 for a review). Such a dark energy model can be characterized by a time-dependent equation of state $w(a) = p_{\text{de}}/\rho_{\text{de}}$ with $w \leq 0$ (the cosmological constant corresponds to $w = -1$). It is useful to treat this as a parametrization to be determined empirically, due to the lack of compelling models for the dark energy (e.g. Turner & White 1997).

The dynamically evolving dark energy affects the expansion rate of the Universe, which in turn alters the redshift evolution of mass clustering. It is well established that weak lensing can directly map the mass distribution along the line of sight by measuring the correlated distortion of images of distant galaxies (see Mellier 1999; Bartelmann & Schneider 2001 for review; and also see, e.g. Hamana et al. 2003; Jarvis et al. 2003; Van Waerbeke & Mellier 2003, and references therein for the state of observations). Future wide-field multicolour surveys are expected to have photometric redshift information for distant galaxies beyond $z = 1$ (see e.g. Massey et al. 2004). This additional information is extremely valuable in that it allows us to recover radial information on the lensing field, which probes the redshift evolution of the expansion history and mass clustering. Because the weak lensing observables are predictable ab initio given a cosmological model, lensing tomography

[★]E-mail: mtakada@hep.upenn.edu (MT); bjain@physics.upenn.edu (BJ)

is a well-grounded means of constraining dark energy evolution (Hu 1999, 2002a,b; Huterer 2002; Futamase & Yoshida 2001; Abazajian & Dodelson 2003; Heavens 2003; Refregier et al. 2004; Benabed & Van Waerbeke 2004; Jain & Taylor 2003; Bernstein & Jain 2004; Simon, King & Schneider 2004). While luminosity distance measures of supernovae are an established direct probe of dark energy (e.g. Chiba & Nakamura 2000; Huterer & Turner 2001; Tegmark 2002; Frieman et al. 2003; Linder 2003), it is important to perform cross checks of various methods to understand systematics and because they have sensitivities to different redshift ranges.

Non-linear gravitational clustering induces non-Gaussianity in the weak lensing fields, even if the primordial fluctuations are Gaussian. This non-Gaussian signal thus provides additional information on structure formation models that cannot be extracted by the widely used two-point statistics such as the power spectrum. The bispectrum, the Fourier counterpart of the three-point correlation function, is the lowest-order statistical quantity to describe non-Gaussianity. Future wide-field surveys promise to measure the bispectrum of lensing fields at high significance, as will be shown here. The primary goal of this paper is to determine the expected accuracy on cosmological parameters from tomography that jointly uses the lensing power spectrum and bispectrum. The lensing bispectrum or skewness have been applied for cosmological parameter estimation in previous studies (Hui 1999; Benabed & Bernardeau 2001; Cooray & Hu 2001a; Refregier et al. 2004).

In this work, we use the lensing bispectra over all triangle configurations available from a given survey to compute the signal-to-noise ratio for the bispectrum measurement. In addition, we use all the cross- and auto-bispectra constructed from the lensing fields in redshift bins. To do this, we correctly take into account the covariance in the analysis. We study all the parameters that the lensing power spectrum and bispectrum are sensitive to and present results for desired parameters with different marginalization schemes.

We employ the cold dark matter (CDM) model to predict the lensing power spectrum and bispectrum for dark energy cosmologies. The parameter constraints derived thus depend on the model of mass clustering (see Jain & Taylor 2003; Bernstein & Jain 2004, for a model-independent method). Hence, we derive the constraints on dark energy parameters marginalized over the other cosmological parameters on which the lensing observables depend. On angular scales below 1° , non-linear evolution leads to a significant enhancement of the bispectrum amplitude (compared to perturbation theory), and is likely to amplify the dark energy dependences (e.g. Hui 1999; Ma et al. 1999). We employ an analytic fitting formula of the mass bispectrum given by Scoccimarro & Couchman (2001; see also Scoccimarro & Frieman 1999) to make model predictions of the lensing bispectrum. Because the physics involved in weak lensing is only gravity, developing an accurate model of the non-linear bispectrum is achievable from N -body simulations, as has been done for the non-linear power spectrum (e.g. Smith et al. 2003, hereafter Smith03).

In addition, tomography of the lensing bispectrum offers the possibility of constraining primordial non-Gaussianity. While CMB observations so far have shown that the primordial fluctuations are close to Gaussian (e.g. Komatsu et al. 2003), it is still worth exploring primordial non-Gaussianity from observations of large-scale structure at low redshifts, as the length-scales probed by these two methods are different. Exploring primordial non-Gaussianity provides useful information on the physics involved in the early Universe, such as particular inflation models (e.g. Wang & Steinhardt 1998; Verde et al. 2000; Komatsu 2001; Dvali, Gruzinov & Zaldarriaga 2003; Zaldarriaga 2003, and references therein). The lensing bispectrum due to primordial non-Gaussianity has a different redshift evolution from that due to the non-Gaussianity of structure formation and, in addition, their configuration dependences differ. Hence, bispectrum tomography can be useful in separating these two contributions. We estimate how measuring the lensing bispectrum from future surveys can constrain the primordial non-Gaussianity.

The structure of this paper is as follows. In Section 2, we present the formalism for computing the power spectrum, bispectrum and cross-spectra of the lensing convergence. The covariance between the bispectra in redshift bins is derived. Section 3 presents the signal-to-noise ratio for measuring the lensing bispectrum for future wide-field surveys. From this estimate, we show how lensing tomography can put constraints on primordial non-Gaussian model. In Section 4, we present the Fisher matrix formalism for lensing tomography. In Section 5 we present the forecasts for constraints on cosmological parameters and the equation of state of dark energy. We conclude in Section 6.

We will use the concordance Λ CDM model with $\Omega_{\text{cdm}} = 0.3$, $\Omega_{\text{b}} = 0.05$, $\Omega_{\text{de}} = 0.65$, $n = 1$, $h = 0.72$ and $\sigma_8 = 0.9$ as supported from the *WMAP* result (Spergel et al. 2003). Ω_{cdm} , Ω_{b} and Ω_{de} are density parameters of the CDM, baryons and the cosmological constant at present, respectively, n is the spectral index of the primordial power spectrum of scalar perturbations, h is the Hubble parameter, and σ_8 is the rms mass fluctuation in spheres of radius $8 h^{-1}$ Mpc.

2 LENSING POWER SPECTRUM AND BISPECTRUM TOMOGRAPHY

2.1 Preliminaries: cosmology

We work in the context of spatially flat CDM models for structure formation. The expansion history of the Universe is given by the scalefactor $a(t)$ in a homogeneous and isotropic universe. The scalefactor during the matter-dominated epoch is determined by density contributions from non-relativistic matter density Ω_{m} (the CDM plus the baryons) and dark energy density Ω_{de} at present, in units of the critical density $3H_0^2/(8\pi G)$, where $H_0 = 100 h \text{ km s}^{-1} \text{ Mpc}^{-1}$ is the Hubble parameter at present. The expansion rate, the Hubble parameter, is given by

$$H^2(a) = H_0^2 \left[\Omega_{\text{m}} a^{-3} + \Omega_{\text{de}} e^{-3 \int_1^a da' (1+w(a'))/a'} \right], \quad (1)$$

where we have employed the normalization $a(t_0) = 1$ today for our convention and $w(a)$ specifies the equation of state for dark energy as

$$w(a) \equiv \frac{p_{\text{de}}}{\rho_{\text{de}}} = -\frac{1}{3} \frac{d \ln \rho_{\text{de}}}{d \ln a} - 1. \quad (2)$$

Note that $w = -1$ corresponds to a cosmological constant. The comoving distance $\chi(a)$ from an observer at $a = 1$ to a source at a is expressed in terms of the Hubble parameter as

$$\chi(a) = \int_a^1 \frac{da'}{H(a')a'^2}. \quad (3)$$

This gives the distance–redshift relation $\chi(z)$ via the relation $1 + z = 1/a$.

Dark energy that has negative pressure ($\rho_{\text{de}} + 3p_{\text{de}} < 0$ as observed today) leads to repulsive gravity, and therefore does not cluster significantly. However, dark energy does affect the growth of mass clustering through its effect on the expansion rate. In linear theory, all Fourier modes of the mass density perturbation, $\delta(\equiv \delta\rho_m/\bar{\rho}_m)$, grow at the same rate: $\tilde{\delta}_k(a) = D(a)\tilde{\delta}_k(a=1)$, where $D(a)$ is the growth factor normalized as $D(a=1) = 1$ and, in the following, the tilde symbol is used to denote the Fourier component. The growth factor can be computed by solving the linearized differential equation, $\ddot{\delta}_k + 2(\dot{a}/a)\dot{\delta}_k - 4\pi G\bar{\rho}_m\delta_k = 0$, where the dot is the derivative with respect to physical time. Hence, the growth suppression rate (growth rate relative to that in a flat, matter-dominated universe), $g(a) = D(a)/a$, can be obtained by solving the differential equation (e.g. Wang & Steinhardt 1998):

$$2\frac{d^2g}{d\ln a^2} + [5 - 3w(a)\Omega_{\text{de}}(a)]\frac{dg}{d\ln a} + 3[1 - w(a)]\Omega_{\text{de}}(a)g(a) = 0, \quad (4)$$

where $\Omega_{\text{de}}(a)$ is the dark energy density parameter at epoch a . We employ the initial conditions of $g = 1$ and $dg/d\ln a = 0$ at $a_i = 1/1100$, which is valid for the dark energy models we consider. Throughout this paper we assume a spatially smooth dark energy component (its spatial fluctuations matter on length-scales comparable with the present-day horizon scale, which are not probed by weak lensing surveys of interest). For example, $g(a)$ for dark energy cosmologies are shown in fig. 2 of Linder & Jenkins (2003).

In this paper we mainly employ the σ_8 normalization for the input linear mass power spectrum, equivalent to setting $D(a=1) = 1$ today. In this case, increasing w from $w = -1$, or equivalently increasing the dark energy contribution at $z > 0$, leads to slower redshift evolution of the growth rate, as structure formation freezes at higher redshift; for example $D_{w=-0.9}(z) > D_{w=-1}(z)$ for $z > 0$. Hence, the mass power spectrum amplitude is greater for $w > -1$ than that for the Λ CDM model at $z > 0$.

2.2 Weak lensing fields

In the context of cosmological gravitational lensing, the convergence field is expressed as a weighted projection of the three-dimensional density fluctuation field between source and observer (e.g. see Bartelmann & Schneider 2001; Mellier 1999, for reviews):

$$\kappa(\boldsymbol{\theta}) = \int_0^{\chi_H} d\chi W(\chi)\delta[\chi, \chi\boldsymbol{\theta}], \quad (5)$$

where $\boldsymbol{\theta}$ is the angular position on the sky, χ is the comoving distance, and χ_H is the distance to the horizon. Note that for a flat universe the comoving angular diameter distance is equivalent to the comoving distance. Following Blandford et al. (1991), Miralda-Escude (1991) and Kaiser (1992), we have used the Born approximation, where the convergence field is computed along the unperturbed path. The lensing weight function $W(\chi)$ is defined as

$$W(\chi) = \frac{3}{2}\Omega_{\text{m}0}H_0^2a^{-1}(\chi)\chi\frac{1}{\bar{n}_g}\int_{\chi}^{\chi_H} d\chi_s p_s(z)\frac{dz}{d\chi_s}\frac{\chi_s - \chi}{\chi_s}, \quad (6)$$

where $p_s(z)$ is the redshift selection function of source galaxies and satisfies the normalization condition $\int_0^{\infty} dz p(z) = \bar{n}_g$, with the average number density per unit steradian \bar{n}_g . Following Huterer (2002), we employ the source distribution given by

$$p_s(z) = \bar{n}_g\frac{z^2}{2z_0^3}e^{-z/z_0}, \quad (7)$$

with $z_0 = 0.5$. As shown in Fig. 1, $p(z)$ peaks at $2z_0 = 1$ and has median redshift of galaxies $z_{\text{med}} = 1.5$.

Future surveys will provide photometric redshift information on source galaxies. This additional information allows us to subdivide the galaxies into redshift bins. The average number density of galaxies in a redshift bin i , defined to lie between the comoving distances χ_i and χ_{i+1} , is given by

$$\bar{n}_i = \int_{\chi_i}^{\chi_{i+1}} d\chi_s p_s(z)\frac{dz}{d\chi_s}. \quad (8)$$

Note that this number density determines the shot noise contamination due to the intrinsic ellipticities of galaxies for the power spectrum measurement in the bin (see equation 14). The convergence field for subsample i is

$$\kappa_{(i)}(\boldsymbol{\theta}) = \int_0^{\chi_H} d\chi W_{(i)}(\chi)\delta[\chi, \chi\boldsymbol{\theta}], \quad (9)$$

with the lensing weight function $W_{(i)}$ given by

$$W_{(i)}(\chi) = \begin{cases} \frac{W_0}{\bar{n}_i}a^{-1}(\chi)\chi\int_{\chi_i}^{\chi_{i+1}} d\chi_s p_s(z)\frac{dz}{d\chi_s}\frac{\chi_s - \chi}{\chi_s}, & \chi \leq \chi_{i+1}, \\ 0, & \chi > \chi_{i+1}, \end{cases} \quad (10)$$

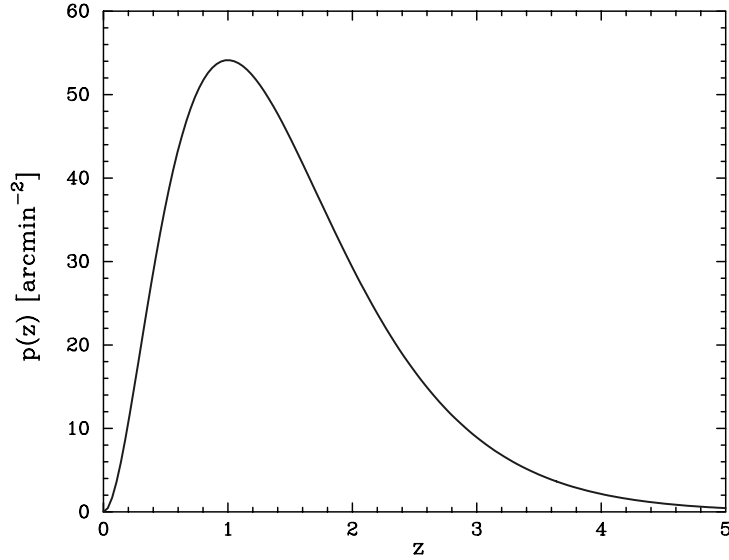


Figure 1. The assumed redshift distribution of source galaxies. The curve is in units of the galaxy number density per arcmin² and normalized as $\int_0^\infty dz p(z) = \bar{n}_g = 100 \text{ arcmin}^{-2}$. This figure is available in colour in the on-line version of the journal on *Synergy*.

where $W_0 = 3/2 \Omega_{m0} H_0^2$. We have ignored possible errors in the photometric redshifts for simplicity. How a dynamically evolving dark energy model changes the lensing weight function is shown in fig. 3 in Huterer (2002). For example, increasing w lowers $W_{(i)}$ – opposite to the dependence of the growth rate of mass clustering (for σ_8 normalization). Thus the dependence of lensing observables on the equation of state is somewhat weakened by these two effects. We have checked that the redshift evolution of the lensing weight function provides the dominant constraints on the equation of state (see also fig. 2 in Abazajian & Dodelson 2003).

2.3 The power spectrum and its covariance

To compute the power spectrum and bispectrum of the convergence, we employ the flat-sky approximation (Blandford et al. 1991; Miralda-Escude 1991; Kaiser 1992). Within this framework the lensing convergence field is decomposed into angular modes based on the two-dimensional Fourier transform: $\kappa(\boldsymbol{\theta}) = \sum_l \tilde{\kappa}_l e^{i\mathbf{l}\cdot\boldsymbol{\theta}}$. The angular power spectrum, $C(l)$, is defined as

$$\langle \tilde{\kappa}_{l_1} \tilde{\kappa}_{l_2} \rangle = (2\pi)^2 \delta^D(\mathbf{l}_{12}) C(l_1), \quad (11)$$

where $\delta^D(\mathbf{l})$ is the Dirac delta function, $\langle \cdot \cdot \rangle$ denotes ensemble averaging, and $\mathbf{l}_{12} = \mathbf{l}_1 + \mathbf{l}_2$.

For lensing tomography, we use all the auto- and cross-power spectra that are constructed from source galaxies divided into redshift bins. The angular power spectrum between redshift bins i and j , $C_{(ij)}(l)$, is given by

$$C_{(ij)}(l) = \int_0^{\chi_H} d\chi W_{(i)}(\chi) W_{(j)}(\chi) \chi^{-2} P_\delta \left(k = \frac{l}{\chi}; \chi \right), \quad (12)$$

where the lensing weight function $W_{(i)}$ is given by equation (10) and $P_\delta(k)$ is the three-dimensional mass power spectrum. Using n_s redshift bins leads to $n_s(n_s + 1)/2$ cross and auto power spectra. Note that we have used Limber's equation (e.g. Kaiser 1992), which is a good approximation over the angular modes we consider, with $50 \leq l \leq 3000$, corresponding to angular scales between 5 arcmin and a few degrees. The non-linear gravitational evolution of $P_\delta(k)$ significantly enhances the amplitude of the lensing power spectrum on angular scales $l \gtrsim 100$ (see Fig. 2). Therefore, we need an accurate model of $P_\delta(k)$, for which we employ the fitting formula proposed by Smith et al. (2003, hereafter Smith03). We assume that the Smith03 formula can be applied to dark energy cosmologies, if we replace the growth factor in the formula with that for a given dark energy cosmology from which we compute the non-linear scale k_{NL} , the effective spectral index n_{eff} and the spectral curvature C used in the formula to obtain the mapping between the linear and non-linear power spectra. The issue of accurate power spectra for general dark energy cosmologies needs to be addressed carefully (see Ma et al. 1999; Huterer 2002, for related discussions). It is encouraging that Linder & Jenkins (2003) find that the mass functions seen in N -body simulations for dark energy cosmologies are well fitted by the universal fitting formula derived in Jenkins et al. (2001), which is derived from the same N -body simulations as used in Smith03.

Measured shear correlations contain a shot-noise contribution from the intrinsic ellipticities of source galaxies. Assuming that the ellipticity distribution is uncorrelated between different galaxies, the observed power spectrum between redshift bins i and j can be expressed as (Kaiser 1992, 1998; Hu 1999)

$$C_{(ij)}^{\text{obs}}(l) = C_{(ij)}(l) + \delta_{ij} \frac{\sigma_\epsilon^2}{\bar{n}_i}, \quad (13)$$

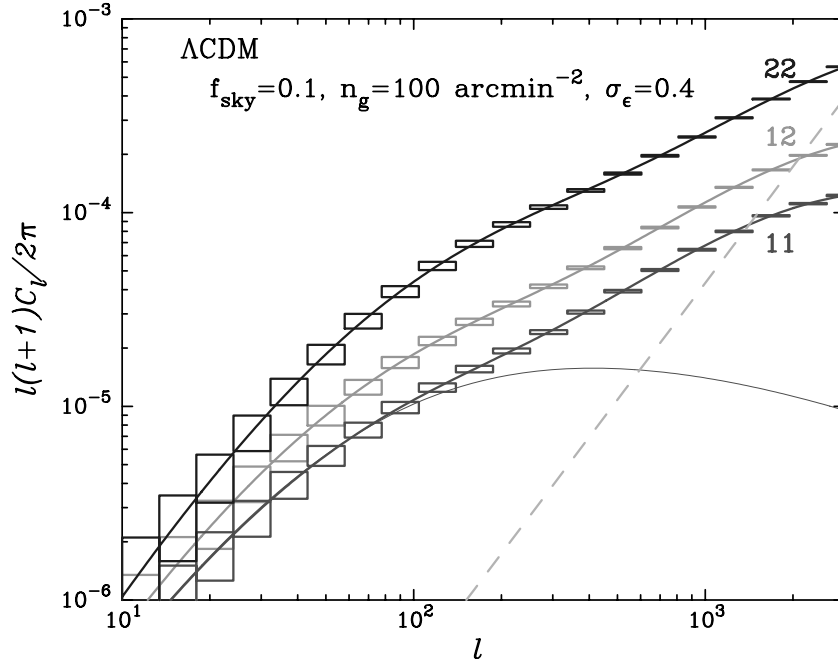


Figure 2. The lensing power spectra constructed from galaxies in two redshift bins, $0 \leq z_1 \leq 1.3$ and $1.3 \leq z_2$. The solid curves are the results for the fiducial Λ CDM model, computed from the Smith03 fitting formula. The boxes show the expected measurement error due to sample variance and intrinsic ellipticities. The sky coverage is $f_{\text{sky}} = 0.1$ and the rms of intrinsic ellipticities, $\sigma_\epsilon = 0.4$. The linear power spectrum for the l bin is shown by the thin solid line to show how significant the non-linear effect is. The dashed curve shows the shot noise contribution to the power spectrum measurement. This figure is available in colour in the on-line version of the journal on *Synergy*.

where \bar{n}_i is the average number density of galaxies in redshift bin i , as given by equation (8). The Kronecker delta function enforces the fact that the cross power spectrum with $i \neq j$ is not affected by shot noise. In this sense, the cross power spectrum is an unbiased estimator of the cosmological signal. We have ignored other possible contaminations such as observational systematics and intrinsic ellipticity alignments (the latter is also likely to be negligible for cross power spectra as discussed in Takada & White 2004).

The power spectrum covariance is needed to understand statistical errors on the power spectrum measurement. Extending the expression in Kaiser (1998) and Scoccimarro, Zaldarriaga & Hui (1999), the covariance between the power spectra $C_{(ij)}(l)$ and $C_{(mn)}(l')$ is

$$\text{Cov} [C_{(ij)}^{\text{obs}}(l), C_{(mn)}^{\text{obs}}(l')] = \frac{2\delta_{ll'}}{(2l+1)\Delta l f_{\text{sky}}} [C_{(im)}^{\text{obs}}(l)C_{(jn)}^{\text{obs}}(l) + C_{(in)}^{\text{obs}}(l)C_{(jm)}^{\text{obs}}(l)] + \frac{1}{4\pi f_{\text{sky}}} \int \frac{d^2\mathbf{l}}{A(l)} \int \frac{d^2\mathbf{l}'}{A(l')} T_{(ijmn)}(\mathbf{l}, -\mathbf{l}, \mathbf{l}', -\mathbf{l}'), \quad (14)$$

where $T_{(ijmn)}$ is the trispectrum of the convergence fields in redshift bins i, j, m and n , f_{sky} is the fraction of sky covered and Δl is the bin width centred at l , so that the area of the shell is $A(l) = 2\pi l \Delta l$. The first term denotes the Gaussian contribution to the covariance, and does not lead to any correlation between the power spectra of different l modes. The second term is the contribution due to the non-Gaussianity of the weak lensing field. We restrict our analysis to angular scales $l \leq 3000$. Over this range, the statistical properties of the lensing fields are quite close to Gaussian (Scoccimarro et al. 1999; White & Hu 2000; Cooray & Hu 2001b). This is physically because the weak lensing field is caused by independent structures at different redshifts along the line of sight and this makes the lensing field close to Gaussian due to the central limit theorem, even though the mass distribution in each redshift slice displays strong non-Gaussianity. In what follows, therefore, we ignore the non-Gaussian contribution to the power spectrum covariance.

Fig. 2 shows the lensing power spectra for two redshift bins, leading to three different power spectra as indicated. The solid curves are the results from the Smith03 fitting formula. We parametrized a lensing survey by the sky coverage $f_{\text{sky}} = 0.1$ ($\approx 4000 \text{ deg}^2$), the galaxy number density $\bar{n}_g = 100 \text{ arcmin}^{-2}$ and the rms of intrinsic ellipticities $\sigma_\epsilon = 0.4$, respectively. It is clear that the power spectrum for higher redshift bin has greater amplitude because of the greater lensing efficiency described by the lensing weight function $W_{(i)}$ (see equation 10). The correlation coefficient between the power spectra of the redshift bins, $R_{ij} = C_{(ij)}(l)/[C_{(ii)}(l)C_{(jj)}(l)]^{1/2}$, quantifies how the power spectra are correlated. Even with only two redshift bins, the power spectra are highly correlated as $R_{12} \sim 0.8$. One thus gains little information from further subdivision of the redshift bins (Hu 1999, 2002a,b). The box around each curve shows the expected measurement error at a given bin of l , which includes the cosmic sample variance and the error due to the intrinsic ellipticities. As can be seen, this type of survey allows the power spectrum measurements with significant signal-to-noise ratio. The dashed curve shows the shot-noise contribution to the power spectrum measurement. The comparison with the power spectrum amplitude clarifies that shot noise becomes dominant over or comparable with sample variance at $l \gtrsim 10^3$. It is worth noting that shot noise only contributes to the Gaussian term in the power spectrum covariance, thus strengthening the case for our Gaussian error assumption (Cooray & Hu 2001b). Finally, to clarify the effect of the non-linear gravitational

clustering, the thin solid curve shows the prediction of $C_{(11)}(l)$ from the linear mass power spectrum: the non-linear effect induces a significant enhancement in the amplitude by about an order of magnitude at $l \gtrsim 100$.

2.4 Convergence bispectrum and its covariance

2.4.1 Definition

In this subsection, we consider tomography with the lensing bispectrum, which is the main focus of this paper. The bispectrum is the lowest-order quantity to extract non-Gaussianity in the weak lensing field, and thus provides additional information on structure formation models relative to the power spectrum (e.g. Takada & Jain 2002, 2003a,b,c, hereafter TJ02 and TJ03a,b,c). For convenience of the following discussion, we start with the definition of the bispectrum based on the harmonic expansion of the convergence field that accounts for the curvature of a celestial sphere (Hu 2000; Komatsu 2002): $\kappa(\boldsymbol{\theta}) = \sum_{lm} \kappa_{lm} Y_{lm}(\boldsymbol{\theta})$. The bispectrum, $B_{(ijk)l_1 l_2 l_3}$, between the convergence fields in redshift bins i, j and k , is defined as

$$\langle \kappa_{l_1 m_1(i)} \kappa_{l_2 m_2(j)} \kappa_{l_3 m_3(k)} \rangle = \begin{pmatrix} l_1 & l_2 & l_3 \\ m_1 & m_2 & m_3 \end{pmatrix} B_{(ijk)l_1 l_2 l_3}, \quad (15)$$

where $\begin{pmatrix} l_1 & l_2 & l_3 \\ m_1 & m_2 & m_3 \end{pmatrix}$ is the Wigner-3j symbol. The triangle condition of $|l_i - l_j| \leq l_k \leq l_i + l_j$ is imposed for all (m_1, m_2, m_3) , and $l_1 + l_2 + l_3 = \text{even}$ is required from statistical parity invariance of the angular correlation.

The relation between the bispectra of the all-sky approach and the flat-sky approximation is given by

$$B_{(ijk)l_1 l_2 l_3} \approx \begin{pmatrix} l_1 & l_2 & l_3 \\ 0 & 0 & 0 \end{pmatrix} \sqrt{\frac{(2l_1 + 1)(2l_2 + 1)(2l_3 + 1)}{4\pi}} B_{(ijk)}(\mathbf{l}_1, \mathbf{l}_2, \mathbf{l}_3). \quad (16)$$

We will use this equation to compute the all-sky lensing bispectrum from the flat-sky bispectrum (see below), with the Wigner-3j symbol, given by the approximation described in Appendix A.

For a given cosmological model, we use the flat-sky approximation to predict the bispectrum as it is sufficiently accurate over angular scales of our interest. Combining the flat-sky approximation and Limber's equation leads to a simple expression for the bispectrum in redshift bins i, j and k , $B_{(ijk)}(\mathbf{l}_1, \mathbf{l}_2, \mathbf{l}_3)$:

$$\langle \tilde{\kappa}_{(i)}(\mathbf{l}_1) \tilde{\kappa}_{(j)}(\mathbf{l}_2) \tilde{\kappa}_{(k)}(\mathbf{l}_3) \rangle = (2\pi)^2 B_{(ijk)}(\mathbf{l}_1, \mathbf{l}_2, \mathbf{l}_3) \delta^D(\mathbf{l}_{123}) \quad (17)$$

with

$$B_{(ijk)}(\mathbf{l}_1, \mathbf{l}_2, \mathbf{l}_3) = \int_0^{\chi_H} d\chi W_{(i)}(\chi) W_{(j)}(\chi) W_{(k)}(\chi) \chi^{-4} B_\delta(\mathbf{k}_1, \mathbf{k}_2, \mathbf{k}_3; \chi), \quad (18)$$

where $\mathbf{k}_i = \mathbf{l}_i/\chi$ and $B_\delta(\mathbf{k}_1, \mathbf{k}_2, \mathbf{k}_3)$ is the bispectrum of the three-dimensional mass fluctuations. Note that the delta function $\delta^D(\mathbf{l}_{123})$ in the bispectrum (17) enforces the condition that the three vectors $\mathbf{l}_1, \mathbf{l}_2$ and \mathbf{l}_3 form a triangle configuration in the Fourier space. From statistical isotropy, the convergence bispectrum is a function of the three parameters that specify the triangle configuration, e.g. l_1, l_2 and l_3 . For n_s redshift bins, n_s^3 lensing bispectra contribute to the Fisher matrix for a given set of (unequal) (l_1, l_2, l_3) .¹ For comparison, there are $n_s(n_s + 1)/2$ power spectra. Note that equations (17) and (18) show there are symmetry relations among the n_s^3 bispectra in an ensemble average sense: e.g. for $n_s = 2$ we have the relations $B_{(112)} = B_{(121)} = B_{(211)}$ and $B_{(122)} = B_{(212)} = B_{(221)}$, but they are different in the sense that their estimators and covariances are different, as shown below.

In the following, we consider two sources for the mass bispectrum B_δ : one is primordial non-Gaussianity, which could be imprinted in the early Universe, and the other is the non-Gaussianity induced by non-linear gravitational clustering from primordial (nearly) Gaussian fluctuations.

2.4.2 Bispectrum from primordial non-Gaussianity

Following Verde et al. (1999), we consider a model in which the primordial gravitational potential $\Phi(\mathbf{x})$ is a linear combination of a Gaussian random field ϕ and a term proportional to the square of the same random field:

$$\Phi(\mathbf{x}) = \phi(\mathbf{x}) + f_{\text{NL}}[\phi^2(\mathbf{x}) - \langle \phi^2(\mathbf{x}) \rangle] \quad (19)$$

where f_{NL} parametrizes the non-Gaussian amplitude: in the limit $f_{\text{NL}} \rightarrow 0$, the field becomes Gaussian. The physical motivation for this model (given that there is a range of possible non-Gaussian models) is that such a non-Gaussian field naturally arises in slow-roll inflation and other inflation models (Luo 1994; Falk, Rangarajan & Srednicki 1993; Gangui et al. 1994, and also see Komatsu 2001 for a review) or in models in which the epoch of reheating has a spatial dependence (Dvali et al. 2003; Zaldarriaga 2003). The Sachs–Wolfe effect measured in the CMB

¹ The number of bispectra is reduced to $n_s(n_s + 1)/2$ and $n_s(n_s + 1)(n_s + 2)/6$ for isosceles triangles, e.g. $l_1 = l_2 \neq l_3$, and equilateral triangles with $l_1 = l_2 = l_3$, respectively.

power spectrum implies $\Phi \sim 10^{-5}$ and the potential remains constant in time on horizon scales. From this amplitude and the current limit on $f_{\text{NL}} < 100$ from the CMB bispectrum measurement (Komatsu et al. 2003), the second term in equation (19) is much smaller than the first term. As long as $\Phi \ll 1$ at a given length-scale, the redshift evolution of Φ obeys linear theory.

A future wide-field lensing survey will enable accurate measurements of the lensing bispectrum down to arcmin scales, as shown below. On scales larger than 1° , the lensing convergence arises from structures in the linear or weakly non-linear regime, so that different Fourier modes are almost uncorrelated. Hence the lensing field retains the imprint of primordial non-Gaussianity. On smaller scales, it remains to be seen how highly non-linear structures show signatures from primordial non-Gaussianity (see Matarrese, Verde & Jimenez 2000, for an analytic discussion).

To consider the effect of primordial non-Gaussianity on weak lensing fields, we need to account for the different evolution of modes inside the horizon. We assume that, in the linear regime, the evolution can be described by the transfer function. Because the density fluctuation field is related to the potential field via the Poissonian equation, the Fourier transform of the density fluctuation field, $\tilde{\delta}(\mathbf{k})$, at epoch z can be expressed as

$$\tilde{\delta}(\mathbf{k}; z) = D(z)\mathcal{M}_k\tilde{\Phi}(\mathbf{k}), \quad (20)$$

with

$$\mathcal{M}_k = -\frac{2}{3H_0^2\Omega_{\text{m}0}}k^2T(k), \quad (21)$$

where $D(z)$ is the linear growth rate and $T(k)$ is the transfer function as given e.g. by the BBKS formula (Bardeen et al. 1986). We assume that the power spectrum of $\tilde{\Phi}$ is given by a single power law, $P_\Phi(k) \propto k^{n-4}$, and the amplitude is typically $k^3P_\Phi \sim 10^{-5}$ as stated above. Hence, the linear mass power spectrum at redshift z is given by $P_\delta^L(k; z) = D(z)^2\mathcal{M}_k^2P_\Phi(k)$. For a plausible range of f_{NL} , the non-Gaussian contribution to the mass power spectrum is much smaller than the Gaussian contribution as stated above, and therefore it is a good approximation to fix the normalization of $P_\delta^L(k)$ from the Gaussian term alone, based on measurements such as the CMB anisotropy or the σ_8 normalization.

Even in the linear regime, the bispectrum of mass fluctuations due to primordial non-Gaussianity at redshift z is given by

$$B_\delta^{\text{NG}}(\mathbf{k}_1, \mathbf{k}_2, \mathbf{k}_3; z) = 2f_{\text{NL}}D^3(z) \left[P_\delta^L(k_1)P_\delta^L(k_2)\frac{\mathcal{M}_{k_3}}{\mathcal{M}_{k_1}\mathcal{M}_{k_2}} + 2 \text{perm.} \right]. \quad (22)$$

Substituting this expression into equation (18) gives the prediction for the lensing bispectrum. We will use the prediction to estimate how a wide-field lensing survey can constrain f_{NL} .

2.4.3 Bispectrum due to gravitational clustering

Even if the primordial fluctuations are Gaussian, non-linear gravitational clustering at low redshifts leads to non-Gaussian features in the mass distribution due to the coupling of different Fourier modes.

In the weakly non-linear regime ($\delta \lesssim 1$), the evolution of mass clustering can be described by perturbation theory (e.g. Bernardeau et al. 2002b). Perturbation theory ceases to be accurate in the non-linear regime ($\delta \gtrsim 1$). Non-linear clustering enhances the amplitude of mass fluctuations which significantly increases the lensing signal on angular scales below a degree, as shown in Fig. 2 (see also Jain & Seljak 1997). Therefore, it is necessary to account for non-linear effects to correctly interpret measurements from lensing surveys. However, an accurate model of the non-linear mass bispectrum is not yet available, in part because the simulations needed to calibrate such model predictions are challenging to carry out: many realizations of high-resolution simulations are needed to calibrate the triangle configuration dependence of the bispectrum. For this study we will use the best available models to clarify the usefulness of bispectrum tomography. While the resulting parameter accuracy forecasts are likely to be adequate, to actually infer the correct values of parameters from measurements, better predictions will be needed.

There are two well-studied analytic models of non-linear clustering that we have implemented: hyper-extended perturbation theory (Scoccimarro & Frieman 1999; Scoccimarro & Couchman 2001) and the dark matter halo approach (e.g. Cooray & Hu 2001a, TJ03b,c, Takada & Hamana 2003 and Cooray & Sheth 2002 for a review). These models are accurate at the 10–30 per cent level in the amplitude of the three-point correlation function (TJ03b,c). In this paper, we employ the fitting formula of Scoccimarro & Couchman for the mass bispectrum, as it makes it feasible to evaluate the Fisher matrix of bispectrum tomography with reasonable computational expense compared to the halo model implementation:

$$B_\delta^{\text{GRAV}}(\mathbf{k}_1, \mathbf{k}_2, \mathbf{k}_3; z) = 2F_2^{\text{eff}}(\mathbf{k}_1, \mathbf{k}_2)P_\delta^{\text{NL}}(k_1; z)P_\delta^{\text{NL}}(k_2; z) + 2 \text{perm.}, \quad (23)$$

with the kernel F_2^{eff} given by

$$F_2^{\text{eff}}(\mathbf{k}_1, \mathbf{k}_2) = \frac{5}{7}a(n_{\text{eff}}, k_1)a(n_{\text{eff}}, k_2) + \frac{1}{2} \left(\frac{k_1}{k_2} + \frac{k_2}{k_1} \right) \frac{(\mathbf{k}_1 \cdot \mathbf{k}_2)}{k_1k_2} b(n_{\text{eff}}, k_1)b(n_{\text{eff}}, k_2) + \frac{2}{7} \frac{(\mathbf{k}_1 \cdot \mathbf{k}_2)^2}{k_1^2k_2^2} c(n_{\text{eff}}, k_1)c(n_{\text{eff}}, k_2). \quad (24)$$

Note that P_{δ}^{NL} in equation (23) is the non-linear mass power spectrum for which we use the Smith03 fitting formula. The fitting functions in F_2^{eff} are given by

$$\begin{aligned} a(n_{\text{eff}}, k) &= \frac{1 + \sigma_8^{-0.2}(z)\sqrt{0.7Q_3(n_{\text{eff}})}(q/4)^{n_{\text{eff}}+3.5}}{1 + (q/4)^{n_{\text{eff}}+3.5}}, \\ b(n_{\text{eff}}, k) &= \frac{1 + 0.4(n_{\text{eff}} + 3)q^{n_{\text{eff}}+3}}{1 + q^{n_{\text{eff}}+3.5}}, \\ c(n_{\text{eff}}, k) &= \frac{1 + \left(\frac{4.5}{1.5+(n_{\text{eff}}+3)^4}\right)(2q)^{n_{\text{eff}}+3}}{1 + (2q)^{n_{\text{eff}}+3.5}}, \end{aligned} \quad (25)$$

where n_{eff} is the effective spectral index of the power spectrum at the scale k defined as $n_{\text{eff}}(k) \equiv d \ln P_{\delta}^L / d \ln k$ [$P_{\delta}^L(k)$ is the linear mass power spectrum]. The quantities q and Q_3 are defined by $q = k/k_{\text{NL}}$ with $(k^3/2\pi^3)D^2(z)P_{\delta}^L(k_{\text{NL}}) = 1$ and $Q_3(n_{\text{eff}}) = (4 - 2^{n_{\text{eff}}})/(1 + 2^{n_{\text{eff}}+1})$, respectively, and $\sigma_8(z) = D(z)\sigma_8$.

One can find that for large length-scales, where $k \ll k_{\text{NL}}$ (or equivalently $q \ll 1$), $a = b = c = 1$ and the bispectrum (23) recovers the tree level perturbation theory prediction. On the other hand, on small scales, $k \gg k_{\text{NL}}$, $a = \sigma_8^{-0.2}(z)\sqrt{0.7Q_3(n_{\text{eff}})}$ and $b = c = 0$, so the bispectrum becomes independent of triangle configuration and thus provides the so-called hierarchical Ansatz. However, it should be noted that a more realistic non-linear clustering likely displays weak violation of the hierarchical Ansatz in the strongly non-linear regimes (TJ03b,c).

It is worth mentioning about how the bispectrum (23) depends on equation of state of dark energy. In the weakly non-linear regime, the dark energy dependence enters into the growth factor only and it does not modify the configuration dependence (as long as we ignore the spatial fluctuations that modify the transfer function on horizon scales, as shown in Caldwell et al. 1998; Ma et al. 1999). In the non-linear regime, the dependence is captured in a complex way through the non-linear power spectrum and $\sigma_8(z)$ and the non-linear scale $k_{\text{NL}}(z)$ in the fitting functions a , b and c . However, the dark energy dependence on the *lensing bispectrum*, obtained after projecting the mass bispectrum with lensing efficiency, is mainly determined by the dependence of the lensing weight function (6).

A comparison of equations (22) and (23) shows the differences between the bispectra due to the primordial non-Gaussianity and gravitational clustering. The first difference is in the redshift dependence: the bispectrum from primordial non-Gaussianity has a slower redshift evolution than the gravitational clustering bispectrum. Thus lensing tomography should be effective in separating these two contributions. The bispectra also differ in the dependence on triangle configuration: the gravity bispectrum has a stronger configuration dependences on large length-scales where the primordial non-Gaussianity is relevant.

Fig. 3 shows the convergence bispectra with two redshift bins against side length l of equilateral triangles, as in Fig. 2. The left-hand panel shows the model predictions from the hyper extended perturbation theory (23), while the right-hand panel shows the predictions from the primordial non-Gaussian model (22) with $f_{\text{NL}} = 1$. For two redshift bins, we have four different lensing bispectra as indicated. For comparison, the thin curve in the left-hand panel shows the lensing bispectrum computed from the perturbation theory of structure formation. It is obvious that the non-linear gravitational clustering significantly enhances the bispectrum amplitude relative to the perturbation theory prediction by more than an order of magnitude at $l \gtrsim 100$. Note that the halo model used in TJ03c provides the similar bispectra to within 25 per cent difference in the amplitude over the range of angular scales we consider. From the right-hand panel, one can find that the amplitude of the bispectrum B_{κ}^{NG} from the primordial non-Gaussian model is much smaller than that from the structure formation bispectrum B_{κ}^{GRAV} over the range of angular scales we consider (this is true even if we use the current upper limit $f_{\text{NL}} \simeq 100$ in Komatsu et al. 2003).

2.4.4 Bispectrum covariance

In this subsection, we derive the covariance of the convergence bispectrum. To do this, we start with considering an estimator of the bispectrum. One practical advantage for measuring the bispectrum (and more generally odd numbered correlation functions) is that the intrinsic ellipticities do not contaminate the measurement, as long as the intrinsic ellipticity distribution is symmetric with zero mean. Thus the measured bispectrum is an unbiased estimator of the cosmological signal:

$$B_{(ijk)}^{\text{obs}}(\mathbf{l}_1, \mathbf{l}_2, \mathbf{l}_3) \approx B_{(ijk)}(\mathbf{l}_1, \mathbf{l}_2, \mathbf{l}_3). \quad (26)$$

It is also worth noting that the B -mode induced by intrinsic ellipticity alignment does not contaminate the bispectrum measurement due to statistical parity invariance (Schneider 2003).

Extending the expression of the bispectrum covariance derived within the full-sky approach (Hu 2000), the covariance between the lensing bispectra (15) in redshift bins can be simply expressed as

$$\begin{aligned} \mathbf{Cov} [B_{l_1 l_2 l_3 (abc)}, B_{l'_1 l'_2 l'_3 (ijk)}] &\approx C_{(ai)}^{\text{obs}}(l_1)\delta_{l_1 l'_1} [C_{(bj)}^{\text{obs}}(l_2)C_{(ck)}^{\text{obs}}(l_3)\delta_{l_2 l'_2}\delta_{l_3 l'_3} + C_{(bk)}^{\text{obs}}(l_2)C_{(cj)}^{\text{obs}}(l_3)\delta_{l_2 l'_3}\delta_{l_3 l'_2}] \\ &\quad + C_{(aj)}^{\text{obs}}(l_1)\delta_{l_1 l'_2} [C_{(bi)}^{\text{obs}}(l_2)C_{(ck)}^{\text{obs}}(l_3)\delta_{l_2 l'_1}\delta_{l_3 l'_3} + C_{(bk)}^{\text{obs}}(l_2)C_{(ci)}^{\text{obs}}(l_3)\delta_{l_2 l'_3}\delta_{l_3 l'_1}] \\ &\quad + C_{(ak)}^{\text{obs}}(l_1)\delta_{l_1 l'_3} [C_{(bi)}^{\text{obs}}(l_2)C_{(cj)}^{\text{obs}}(l_3)\delta_{l_2 l'_1}\delta_{l_3 l'_2} + C_{(bj)}^{\text{obs}}(l_2)C_{(ci)}^{\text{obs}}(l_3)\delta_{l_2 l'_2}\delta_{l_3 l'_1}]. \end{aligned} \quad (27)$$

For finite sky coverage, the bispectrum covariance scales as f_{sky}^{-1} . We have ignored the non-Gaussian contributions to the covariance that arise from the connected three-, four- and six-point functions of the convergence field – see discussion for the power spectrum following equation (14). This is in part verified by examining the ratio of the non-Gaussian to the Gaussian contribution to the covariance. For example, this

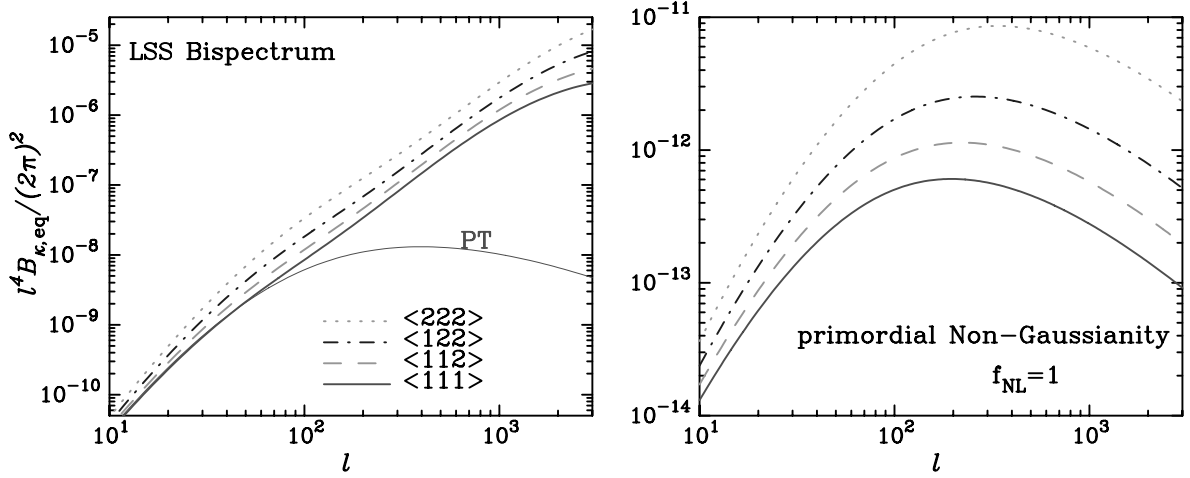


Figure 3. Left-hand panel: the convergence bispectra with two redshift bins for equilateral triangles, plotted against triangle side length. For two redshift bins, there are 4 different bispectra, as indicated. For comparison the thin solid curve shows the perturbation theory prediction for $B_{(111)}$. Non-linear clustering significantly enhances the bispectrum amplitude for $l \gtrsim 100$. Right-hand panel: a similar plot, but for the bispectra due to primordial non-Gaussianity, which are computed from equation (22). The non-Gaussian parameter f_{NL} is taken to be l . This figure is available in colour in the on-line version of the journal on *Synergy*.

ratio for one of these non-Gaussian terms is given by B^2/C_i^3 , and Figs 2 and 3 show that this is much smaller than unity over angular scales of interest. The Kronecker delta functions such as $\delta_{l_1 l'_1} \delta_{l_2 l'_2} \delta_{l_3 l'_3}$ in the equation above guarantee that the bispectra of different triangles are uncorrelated, which makes the Fisher matrix analysis significantly simplified. Note that, on the other hand, the bispectra in different redshift bins are highly correlated.

In the following Fisher matrix analysis, we impose the condition $l_1 \leq l_2 \leq l_3$ so that every triangle configuration is counted once. This condition leads to the following expression for the covariance:

$$\mathbf{Cov}[B_{l_1 l_2 l_3 (abc)}, B_{l'_1 l'_2 l'_3 (ijk)}] \approx \Delta(l_1, l_2, l_3) f_{\text{sky}}^{-1} C_{(ai)}^{\text{obs}}(l_1) C_{(bj)}^{\text{obs}}(l_2) C_{(ck)}^{\text{obs}}(l_3) \delta_{l_1 l'_1} \delta_{l_2 l'_2} \delta_{l_3 l'_3}, \quad (28)$$

where $\Delta(l_1, l_2, l_3) = 1$ if all l 's are different, $\Delta(l_1, l_2, l_3) = 2$ if two l 's are repeated and $\Delta(l_1, l_2, l_3) = 6$ if $l_1 = l_2 = l_3$, respectively. The observed power spectrum is given by equation (13). Strictly speaking, although equation (28) is correct only for $l_1 \neq l_2 \neq l_3$ when we consider redshift bins, we checked that it is a good approximation for the Fisher matrix analysis that follows, because triangles with $l_1 \neq l_2 \neq l_3$ provide the dominant contribution over angular scales of interest. Finally, equation (28) shows that for two redshift bins we have the equality $B_{(112)} = B_{(121)} = B_{(211)}$ (similar conditions hold for other indices) as stated below equation (18), but their covariances are indeed different for a general set of (l_1, l_2, l_3) .

3 SIGNAL-TO-NOISE RATIO FOR THE BISPECTRUM

Before going to parameter accuracy forecasts, we examine how feasible it is to simply measure a non-zero convergence bispectrum from a wide-field lensing survey. Given the bispectrum covariance (28), the cumulative signal-to-noise ratio (S/N) for measuring the bispectra in redshift bins can be expressed as

$$\left(\frac{S}{N}\right)^2 = \sum_{l_{\min} \leq l_1 \leq l_2 \leq l_3 \leq l_{\max}} \sum_{(i,j,k),(a,b,c)} B_{l_1 l_2 l_3 (ijk)} \{\mathbf{Cov}[B_{l_1 l_2 l_3 (ijk)}, B_{l_1 l_2 l_3 (abc)}]\}^{-1} B_{l_1 l_2 l_3 (abc)}, \quad (29)$$

where $\{\mathbf{Cov}\}^{-1}$ denotes the inverse of the covariance matrix, and l_{\min} and l_{\max} denote the minimum and maximum multipole moments considered. The condition $l_1 \leq l_2 \leq l_3$ is imposed, as stated above. Each of the labels (a, b, c) and (i, j, k) denote redshift bins running over $1, \dots, n_s$, thus providing contributions from n_s^3 bispectra to the S/N . Given a survey that probes l up to l_{\max} , a rough estimate of the S/N is

$$\begin{aligned} \left(\frac{S}{N}\right)^2 &\sim f_{\text{sky}} l_{\max}^6 \begin{pmatrix} l_{\max} & l_{\max} & l_{\max} \\ 0 & 0 & 0 \end{pmatrix}^2 \frac{B(l_{\max})^2}{C(l_{\max})^3} \sim f_{\text{sky}} l_{\max}^2 Q_{\kappa}^2 [l_{\max}^2 C(l_{\max})] \\ &\sim 10^5 \left(\frac{f_{\text{sky}}}{0.1}\right) \left(\frac{l_{\max}}{10^3}\right)^2 \left(\frac{Q_{\kappa}}{100}\right)^2 \left[\frac{l_{\max}^2 C(l_{\max})}{10^{-4}}\right], \end{aligned} \quad (30)$$

where we have used equation (16) and $\sum_{l_1, l_2, l_3 \leq l_{\max}} \sim l_{\max}^3$, $\begin{pmatrix} l & l & l \\ 0 & 0 & 0 \end{pmatrix} \sim l^{-1}$ for $l \gg 1$ and introduced the reduced bispectrum Q_{κ} defined as $Q_{\kappa} \sim B(l)/[C(l)]^2$, often used in the literature (e.g. TJ03c). Note that in the estimate above we ignored the shot-noise contribution of intrinsic ellipticities to the covariance, and thus the estimate overestimates the S/N (see Fig. 5, later). As implied from Figs 2 and 3 (also see fig. 6 in TJ03c), a plausible model for the convergence bispectrum leads to $60 \lesssim Q_{\kappa} \lesssim 150$ for $l \gtrsim 100$ (corresponding to $\theta \lesssim 1^\circ$) for the Λ CDM

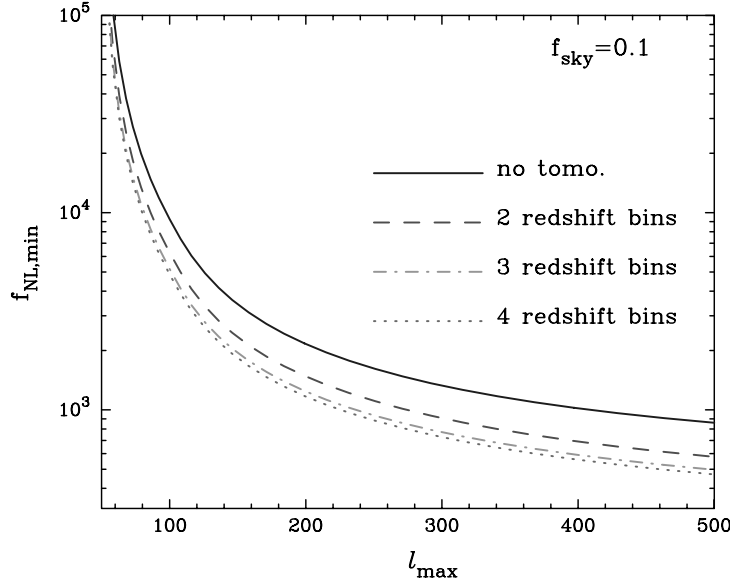


Figure 4. The minimum value of f_{NL} in the primordial non-Gaussian model such that the lensing bispectrum is detectable with $S/N \geq 1$, for a survey with $f_{\text{sky}} = 0.1$. It is plotted against the maximum multipole moment l_{max} . Here we ignore the contribution from non-linear gravitational clustering. Note that f_{NL} scales as $f_{\text{sky}}^{-1/2}$. The different curves show the results for varying numbers of redshift bins used. This figure is available in colour in the on-line version of the journal on *Synergy*.

model. This rough estimate shows that a future survey with $f_{\text{sky}} = 0.1$ would allow for a detection with $S/N \sim 300$ for $l_{\text{max}} = 10^3$, if we combine the information from all triangle configurations available.

We give below a more quantitative S/N estimate for measuring the convergence bispectrum. As described in Section 2.4.2 and 2.4.3, there are two cosmological contributions to the lensing bispectrum, due to the primordial non-Gaussianity and gravitational clustering. The observed bispectrum can be expressed as $B_{\kappa} = B_{\kappa}^{\text{NG}} + B_{\kappa}^{\text{GRAV}}$.

In Fig. 4 we examine the smallest f_{NL} against the maximum multipole moment l_{max} , defined so that the lensing bispectrum is detectable with $S/N \geq 1$. We compute this f_{NL} by setting $B_{\kappa} = B_{\kappa}^{\text{NG}}$ (that is, we ignore the contamination from the bispectrum induced by gravitational clustering B_{κ}^{GRAV}). The sky coverage is taken to be $f_{\text{sky}} = 0.1$ and the minimum multipole moment $l_{\text{min}} = 50$ so that $l_{\text{min}} \sim 10 \times 2\pi / \sqrt{4\pi f_{\text{sky}}}$. The figure shows that the tomography of the lensing bispectrum can lower the f_{NL} value, reflecting the fact that n_s^3 bispectra of the tomography provide additional information on the S/N . As can be seen, f_{NL} is mainly determined by modes with $l \lesssim 100$, due to the high- k suppression of the kernel \mathcal{M}_k in the 3D mass bispectrum (see equation 21 and fig. 1 in Verde et al. 2000). In addition, at higher l the structure formation bispectrum is more dominant (see Fig. 3). Therefore, focusing on large angular scales $\gtrsim 1^\circ$ is probably an appropriate strategy for constraining primordial non-Gaussianity.

The strongest constraint is $f_{\text{NL}} \approx 150 f_{\text{sky}}^{-1/2}$ for $l_{\text{max}} = 500$ and four redshift bins. This result is comparable to the forecast from the galaxy bispectrum measurement from the SDSS/2dF surveys in Verde et al. (2000), where the range $f_{\text{NL}} = 10^3 - 10^4$ was derived (for $f_{\text{sky}} = 10^{-5} - 0.25$ for galaxy catalogues). Unless an almost all-sky lensing survey is available, the CMB bispectrum is likely to provide more stringent constraint on f_{NL} , as shown by the *WMAP* result, $-59 < f_{\text{NL}} < 134$ at 95 per cent confidence, in Komatsu et al. (2003). Hence, we will ignore the primordial non-Gaussian contribution in the following analysis. Only if a significantly deeper all-sky lensing survey is feasible would it be worth returning to this question and exploring measurement strategy.

Fig. 5 shows the S/N for measuring the lensing bispectrum due to structure formation, B_{κ}^{GRAV} . Note that for $l_{\text{max}} \geq 300$ we used a binning of l in the S/N evaluation as described below (see equation 35), because the direct summation over l values is computationally time-consuming for large l_{max} . It is obvious that a survey with $f_{\text{sky}} = 0.1$ allows a significant detection of the lensing bispectrum with $S/N \gtrsim 10$ for $l_{\text{max}} \gtrsim 300$. Bispectrum tomography leads to only slight improvement in the S/N value. For comparison, the top thin curve shows the corresponding S/N for measuring the power spectrum (PS) for two redshift bins, which is roughly estimated as $(S/N)_{\text{PS}} \sim f_{\text{sky}}^{-1/2} l_{\text{max}} \sim 316 (f_{\text{sky}}/0.1)^{-1/2} (l_{\text{max}}/1000)$ (the shot noise is ignored). It is apparent that the S/N values for power spectrum and bispectrum become comparable at $l_{\text{max}} \sim 1000$. Further, the bispectrum S/N displays stronger dependence on l_{max} (roughly $S/N \propto l_{\text{max}}^2$ around $l_{\text{max}} \sim 1000$) than seen in power spectrum, because the bispectrum measurement is contributed from l_{max}^3 triangles, while the power spectrum from different l_{max} modes.

4 FISHER MATRIX ANALYSIS FOR LENSING TOMOGRAPHY

We will use the Fisher matrix formalism (see Tegmark, Taylor & Heavens 1997, for a review), to examine how tomography with the lensing power spectrum and bispectrum can constrain cosmological parameters and the equation of state of dark energy.

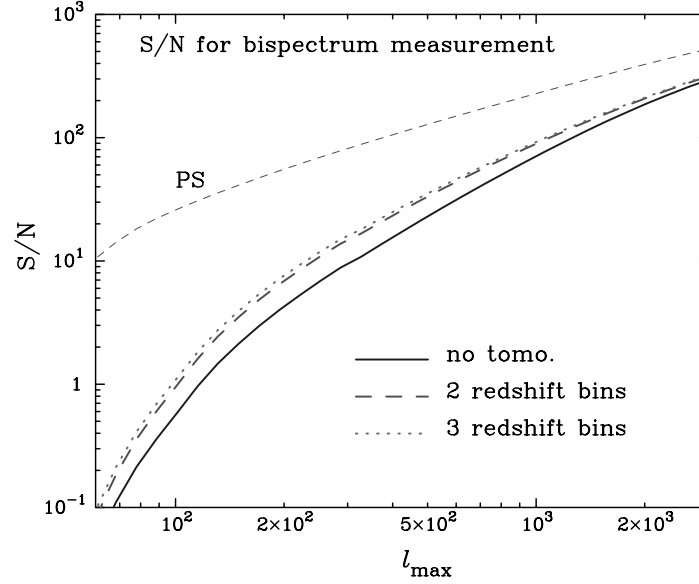


Figure 5. Signal-to-noise ratio estimate for measuring the lensing bispectrum against the maximum multipole moment l_{\max} , as in the previous figure. We consider the bispectrum due to structure formation and ignore the contribution from primordial non-Gaussianity. For comparison, the thin dashed curve shows the signal-to-noise for the power spectrum for two redshift bins. It is clear that l_{\max}^3 triangles allow significant S/N for the bispectrum measurement comparable with that for power spectrum at $l_{\max} \gtrsim 1000$. This figure is available in colour in the on-line version of the journal on *Synergy*.

4.1 Methodology

Given a data vector \mathbf{x} , the Fisher information matrix describes how the errors propagate into the precision on parameters p_α . The Fisher matrix is given by

$$F_{\alpha\beta} = - \left\langle \frac{\partial^2 \ln L}{\partial p_\alpha \partial p_\beta} \right\rangle, \quad (31)$$

where L is the likelihood function of the data set \mathbf{x} given the true parameters p_1, \dots, p_α . The partial derivative with respect to a parameter p_α is evaluated around the fiducial model. The Fisher matrix quantifies the best statistical errors achievable on parameter determination with a given data set: The variance of an unbiased estimator of a parameter p_α obeys the inequality:

$$\langle \Delta p_\alpha^2 \rangle \geq (\mathbf{F}^{-1})_{\alpha\alpha}, \quad (32)$$

where (\mathbf{F}^{-1}) denotes the inverse of the Fisher matrix and Δp_α is the relative error on parameter p_α around its fiducial value. Note that this condition includes marginalization over the other parameters p_β ($\alpha \neq \beta$).

First, we consider power spectrum tomography. Assuming the likelihood function for the lensing power spectrum to be Gaussian, the Fisher matrix can be expressed as

$$F_{\alpha\beta}^{\text{ps}} = \sum_{l=\min(i,j),(m,n)}^{l_{\max}} \sum \frac{\partial C_{(ij)}(l)}{\partial p_\alpha} \{ \mathbf{Cov} [C_{(ij)}(l), C_{(mn)}(l)] \}^{-1} \frac{\partial C_{(mn)}(l)}{\partial p_\beta}, \quad (33)$$

where the power spectrum covariance is given by equation (14) and $\{\mathbf{Cov}\}^{-1}$ denotes the inverse matrix. In the Fisher matrix evaluation above, we consider $n_s(n_s + 1)/2$ cross- and auto-power spectra taken from n_s redshift bins. We will use the power spectrum in 100 bins in l rather than at every multipole moment. We checked that the binning makes no large difference on our results, since the lensing power spectrum does not have any complex features.

Similarly, we assume that the likelihood function for the lensing bispectrum is close to Gaussian. The Fisher matrix for bispectrum tomography is then given by

$$F_{\alpha\beta}^{\text{bisp}} = \sum_{l_{\min} \leq l_1 \leq l_2 \leq l_3 \leq l_{\max}} \sum_{(i,j,k),(a,b,c)} \frac{\partial B_{l_1 l_2 l_3}(ijk)}{\partial p_\alpha} \{ \mathbf{Cov} [B_{l_1 l_2 l_3}(ijk), B_{l_1 l_2 l_3}(abc)] \}^{-1} \frac{\partial B_{l_1 l_2 l_3}(abc)}{\partial p_\beta}, \quad (34)$$

where the bispectrum covariance is given by equation (27) and we have imposed the condition $l_1 \leq l_2 \leq l_3$ so that every triangle configuration is counted once. There are $\sim 10^9$ triangles for $l_{\max} = 3000$, hence it is computationally intractable to compute the contributions from every triangle. We bin l_1 and l_2 , and use the approximation:

$$F_{\alpha\beta}^{\text{bisp}} = \sum_{l'_1} \sum_{l'_2} \Delta l_1 \Delta l_2 \sum_{l_3} \sum_{(i,j,k),(a,b,c)} \frac{\partial B_{l_1 l_2 l_3}(ijk)}{\partial p_\alpha} \{ \mathbf{Cov} [B_{l_1 l_2 l_3}(ijk), B_{l_1 l_2 l_3}(abc)] \}^{-1} \frac{\partial B_{l_1 l_2 l_3}(abc)}{\partial p_\beta}, \quad (35)$$

where l'_1, l'_2 denote the binned values of l_1 and l_2 (we will use 100 bins in the following results). Note that we continue to use a direct summation over l_3 so that we can correctly account for the condition that the Wigner 3- j symbol is non-vanishing for $l_1 + l_2 + l_3 = \text{even}$ and vanishes for $l_1 + l_2 + l_3 = \text{odd}$, where l_1 and l_2 are now the central values in the bin. We checked that our results are not sensitive to this binning, because the lensing bispectrum is smooth within the bin widths used.

We next consider the Fisher information matrix for a joint measurement of the lensing power spectrum and bispectrum. To do this requires a knowledge of the cross covariance between measurements of the power spectrum and bispectrum, which quantifies how the two observables are correlated. However, the covariance has no Gaussian contribution expressed in terms of products of the power spectrum, and arises from the five-point function of the lensing fields. Hence, we ignore the cross covariance for the consistency of the procedure we have taken: the Fisher matrix for the joint measurement can then be approximated by

$$F_{\alpha\beta} \approx F_{\alpha\beta}^{\text{ps}} + F_{\alpha\beta}^{\text{bisp}}. \quad (36)$$

It is useful to consider constraint ellipses in a two-parameter subset of the full parameter space. These are obtained by projection of the higher dimensional ellipsoids, as the projected ellipses include marginalization over the other parameter uncertainties. Assuming that the form of the parameter likelihood function is approximated by a multivariate Gaussian function, the projected likelihood function for the two parameters p_α and p_β is given by (e.g. Matsubara & Szalay 2002):

$$\mathcal{L}(p_\alpha, p_\beta) \propto \exp \left\{ -\frac{1}{2} (\Delta p_\alpha \Delta p_\beta) \begin{bmatrix} (\mathbf{F}^{-1})_{\alpha\alpha} & (\mathbf{F}^{-1})_{\alpha\beta} \\ (\mathbf{F}^{-1})_{\alpha\beta} & (\mathbf{F}^{-1})_{\beta\beta} \end{bmatrix}^{-1} \begin{pmatrix} \Delta p_\alpha \\ \Delta p_\beta \end{pmatrix} \right\}, \quad (37)$$

where the normalization factor is determined to satisfy $\int \Delta p_\alpha \Delta p_\beta \mathcal{L} = 1$ and $[\dots]^{-1}$ denotes the inverse matrix. When many parameters are considered (we will use up to eight parameters), the Fisher matrix formalism has considerable computational advantages over a grid-based search in the likelihood space. Finally, the correlation coefficient, which quantifies how the constraints on parameters p_α and p_β are degenerate with each other, is defined as

$$r(p_\alpha, p_\beta) = \frac{(\mathbf{F}^{-1})_{\alpha\beta}}{\sqrt{(\mathbf{F}^{-1})_{\alpha\alpha}(\mathbf{F}^{-1})_{\beta\beta}}}. \quad (38)$$

If $|r| = 1$, the parameters constraints are totally degenerate, while $r = 0$ means they are uncorrelated.

4.2 The parameter space and fiducial model

We restrict our analysis to a flat CDM universe, supported by CMB observations (e.g. Spergel et al. 2003). The parameter forecasts derived are sensitive to the parameter space used and to whether constraint on a given parameter are obtained by marginalizing over other parameter uncertainties. We mainly use seven parameters which determine the lensing observables within the CDM model: $\Omega_{\text{de}}, w_0, w_a, \sigma_8, n, \Omega_{\text{b}} h^2$ and h , where Ω_{de} and Ω_{b} are the density parameters of dark energy and baryons, n is the spectral index of primordial scalar perturbations, h is the Hubble parameter, and σ_8 is the rms mass fluctuation in a sphere of radius $8 h^{-1}$ Mpc. We use a simple parametrization of the equation of state of dark energy: $w(a) = w_0 + w_a(1 - a)$ (Turner & White 1997; Linder 2003). Note that we use $\Omega_{\text{b}} h^2$ rather than Ω_{b} , because $\Omega_{\text{b}} h^2$ is directly probed by the CMB observations and we will use its prior constraint in the Fisher analysis. For the input linear mass power spectrum, we employ the BBKS transfer function (Bardeen et al. 1986) with the shape parameter given by Sugiyama (1995), which accounts for the baryon contribution. We thus ignore the effect of dark energy spatial fluctuations on the transfer function. For slowly varying dark energy models with $w \leq -0.6$ (the rough current limit from observations, Perlmutter, Turner & White 1999b), the BBKS approximation is reliable on scales probed by weak lensing surveys. Note that dark energy clustering affects horizon scales, and it therefore modifies the *COBE* normalization through changes to the Sachs–Wolfe effect and the integrated Sachs–Wolfe effect (Caldwell et al. 1998; Ma et al. 1999; Hu 2002a). For precise comparisons with data, we will need more accurate transfer function as given by CMBFAST (Seljak & Zaldarriaga 1996). Finally, in this paper we ignore the possible effect of massive neutrinos on the mass power spectrum (see e.g. Hu 2002a; Abazajian & Dodelson 2003).

The Fisher matrix formalism assesses how well lensing observables can distinguish the true (‘fiducial’) model of the Universe from other models. The results we obtain depend upon the fiducial model. We use the currently concordant flat Λ CDM model with $\Omega_{\text{de}} = 0.65, w_0 = -1, w_a = 0, \sigma_8 = 0.9, n = 1, \Omega_{\text{b}} = 0.05$ and $h = 0.72$, which is consistent with the recent *WMAP* results (Spergel et al. 2003). To compute the Fisher matrix, we need to choose steps in parameter directions to compute the numerical derivatives. We choose the steps to be 5 per cent in the parameter values, except for $\Delta w_a = \pm 0.1$; two-side numerical derivatives are used. We will pay special attention to how parameters $\Omega_{\text{de}}, w_0, w_a$ and σ_8 can be constrained from lensing tomography. On the other hand, we will employ prior information on $n\Omega_{\text{b}} h^2$ and h , expected from measurements of the CMB temperature and polarization by the *Planck* satellite mission (e.g. Eisenstein, Hu & Tegmark 1999). Assuming Gaussian priors, we add the diagonal component $(F_{\text{prior}})_{\alpha\beta} = \delta_{\alpha\beta} \sigma(p_\alpha)^{-2}$ to the Fisher matrix. Note that we do not employ any priors to the parameters $\Omega_{\text{de}}, w_0, w_a$ and σ_8 and thus the following results are conservative (see Fig. 8, later, for the joint parameter forecasts using lensing tomography and the CMB).

5 RESULTS: COSMOLOGICAL CONSTRAINTS

We consider three scenarios for constraining cosmological parameters: using the lensing power spectrum and bispectrum without any tomography, tomography in two redshift bins, and tomography in three redshift bins. Fig. 6 shows the resulting constraint ellipses in the parameter

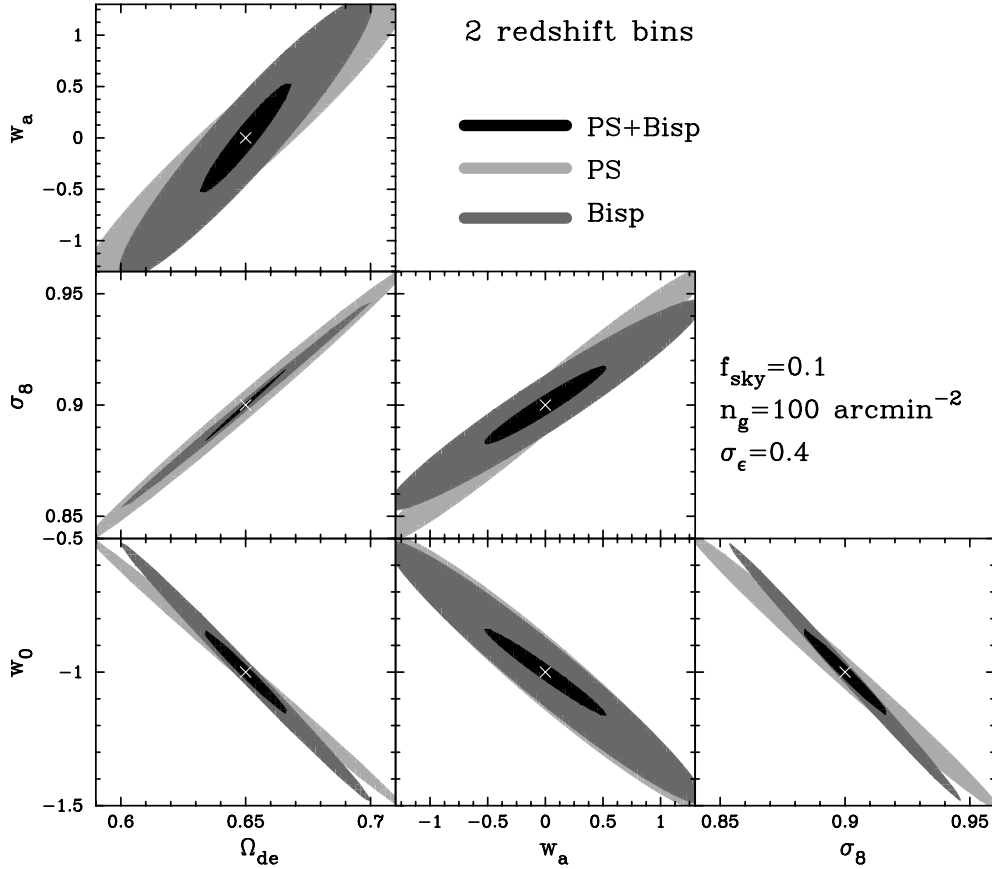


Figure 6. Projected 68 per cent confidence level (CL) constraints in the parameter space of Ω_{de} , w_0 , w_a and σ_8 from the lensing power spectrum and the bispectrum in two redshift bins, as indicated. We employ 7 cosmological parameters in the Fisher matrix analysis. The results shown are obtained assuming priors on n , $\Omega_b h^2$ and h expected from the *Planck* mission. The sky coverage and number density are taken to be $f_{\text{sky}} = 0.1$ and $n_g = 100 \text{ arcmin}^{-2}$, and angular modes $50 \leq l \leq 3000$ are used. It is clear that bispectrum tomography can improve parameter constraints significantly, typically by a factor of 3, compared to just power spectrum tomography. This figure is available in colour in the on-line version of the journal on *Synergy*.

space of Ω_{de} , w_0 , w_a and σ_8 , corresponding to the 68 per cent confidence level ($\Delta\chi^2 = 2.3$), marginalized over the parameters Ω_b , n and h . We consider angular scales $50 \leq l \leq 3000$ and assume the priors $\sigma(\ln \Omega_b h^2) = 0.010$, $\sigma(n) = 0.008$ and $\sigma(h) = 0.13$, expected from the *Planck* mission (see table 2 in Eisenstein et al. 1999). Each redshift bin is chosen so as to have equal number density of galaxies; $0 \leq z \leq 1.3$ and $1.3 \leq z$ for the galaxy distribution shown in Fig. 1. One can see that bispectrum tomography provides additional information on the parameters relative to power spectrum tomography. In particular, one striking result is that the parameter constraints from bispectrum tomography alone are comparable with those from power spectrum tomography. As a result, combining the two can significantly improve parameter determination by a factor of 3, because of their complementarity. For example, the equation of state parameters are constrained as $\sigma(w) = 0.034 f_{\text{sky}}^{-1/2}$ and $\sigma(w_a) = 0.11 f_{\text{sky}}^{-1/2}$. There are two essential features needed to obtain these results. First, we considered all triangle configurations ($\sim 10^9$ triangles) available from a range of angular scales we consider, which leads to a significant gain in S/N . Secondly, we considered all the cross- and auto-spectra constructed from the redshift bins, providing three power spectrum and eight bispectrum contributions to the Fisher matrix.

The correlation coefficients of the Fisher matrix elements quantify how the parameter constraints are degenerate. From the definition (38), we find the dark energy parameters are highly correlated as $r(\Omega_{\text{de}}, w_0) = -0.98$, $r(\Omega_{\text{de}}, w_a) = 0.95$ and $r(w_0, w_a) = -0.97$. It is also worth noting the importance of the marginalization in the Fisher matrix formalism. If we fix Ω_b , n and h to their fiducial values, the constraints improve significantly: $\sigma(\Omega_{\text{de}}) = 0.0031$, $\sigma(w_0) = 0.038$, $\sigma(w_a) = 0.15$ and $\sigma(\sigma_8) = 0.0035$ compared to the errors shown in Table 1.

Table 1 gives the $1\text{-}\sigma$ errors on parameters for three cases: no tomography, tomography with two redshift bins, and tomography with three redshift bins. Clearly tomography leads to significant improvements in parameter accuracies. For the equation of state parameters w_0 and w_a , the improvement in the $1\text{-}\sigma$ errors is a factor of 10. As stressed in Hu (1999), on the other hand, fine divisions of the galaxy redshift distribution for lensing tomography does not give much additional information. This can be seen from Fig. 7, which shows the results for three redshift bins, $0 \leq z \leq 1$, $1 \leq z \leq 1.7$ and $z \geq 1.7$: in this case, we considered 27 bispectra and six power spectra in the Fisher matrix analysis. The constraints on the parameters are improved by 15–20 per cent.

As shown in Figs 6 and 7, lensing tomography alone leads to degenerate constraints on Ω_{de} and the equation of state parameters w_0 and w_a . Therefore, external information on these parameters from other methods such as observations of CMB, supernovae and galaxy redshift surveys is valuable in that it allows us to break the degeneracies. This is investigated in Fig. 8, which shows how the constraint ellipses in the

Table 1. Summary of parameter constraints from lensing tomography of the power spectrum (PS), the bispectrum (Bisp) and both measurements (PS + Bisp). All errors are 1σ level and include marginalization over the other parameters. Note that we have used $f_{\text{sky}} = 0.1$ and all the 1σ errors scale as $\propto f_{\text{sky}}^{-1/2}$. The values in the brackets for three redshift bins show the constraints when we combine lensing tomography and CMB observations (see Fig. 8 in more detail).

Quantity	Parameter estimation								
	No tomography			Two redshift bins			Three redshift bins		
	PS	Bisp	PS + Bisp	PS	Bisp	PS + Bisp	PS	Bisp	PS + Bisp
$\sigma(\Omega_{\text{de}})$	0.14	0.13	0.023	0.043	0.034	0.012	0.024	0.020	0.0098 (0.0046)
$\sigma(\sigma_8)$	0.12	0.12	0.023	0.041	0.031	0.012	0.025	0.020	0.0098
$\sigma(w_0)$	4.0	3.6	1.1	0.34	0.32	0.11	0.20	0.21	0.092 (0.046)
$\sigma(w_a)$	20	15	5.1	0.93	0.91	0.36	0.65	0.71	0.31 (0.14)

subspace of $(\Omega_{\text{de}}, w_0, w_a)$ change when we combine the constraints from lensing tomography and CMB. To compute the Fisher matrix from measurements of the CMB temperature and polarization power spectra and the cross spectrum, we assumed the experimental specifications of the *Planck* 143- and 217-GHz channels with 65 per cent sky coverage and assumed a spatially flat universe, no massive neutrinos, no running tilt and no gravity waves. However, we include the dependence of the dark energy equation of state, which modifies the CMB power spectra through the change of the angular diameter distance to the last scattering surface (we ignored its spatial fluctuations).

In this case, the CMB power spectra are specified by eight parameters $(\Omega_{\text{de}}, w_0, w_a, \delta_\zeta, n, \Omega_b h^2, h, \tau)$ and have been computed using CMBFAST version 4.5 (Seljak & Zaldarriaga 1996). δ_ζ is the amplitude of the primordial curvature fluctuation and τ denotes the optical depth (their fiducial values are taken to be $\delta_\zeta = 4.56 \times 10^{-5}$ and $\tau = 0.15$). Likewise, to compute the Fisher matrix from lensing tomography, we employed the δ_ζ normalization of the mass power spectrum instead of the σ_8 normalization for the consistency. Fig. 8 shows that combining the constraints from CMB measurements and lensing tomography significantly improves the dark energy constraints, yielding $\sigma(\Omega_{\text{de}}) = 4.6 \times 10^{-3}$, $\sigma(w_0) = 0.046$ and $\sigma(w_a) = 0.14$. Note that the results shown are derived by adding the two (7×7) Fisher matrices from lensing tomography and the CMB spectra, including the marginalization over the optical depth. It is also worth noting that the CMB measurements can better constrain the other parameters $(\delta_\zeta, \Omega_b, n, h)$ than lensing tomography, which is part of the reason for the improvement in Fig. 8.

Fig. 9 shows forecasts of the dark energy constraints expected from the *SNAP* survey of Type Ia supernova measurement (E. Linder, private communication) and its lensing survey. We assumed the sky coverage $f_{\text{sky}} = 0.01$ for the *SNAP* weak lensing survey (see Massey et al. 2004; Refregier et al. 2004). It is again apparent that a joint analysis of weak lensing and supernovae significantly improves the parameter errors due to their complementarity: the errors become $\sigma(\Omega_{\text{de}}) = 6.7 \times 10^{-3}$, $\sigma(w_0) = 0.061$ and $\sigma(w_a) = 0.32$. Moreover, this result can be further improved by combining with the CMB constraints, which gives (for $f_{\text{sky}} = 0.01$): $\sigma(w_0) = 0.042$ and $\sigma(w_a) = 0.15$.

5.1 Constraints on running spectral index

Next we examine how lensing observations can probe the running spectral index of primordial scalar perturbations, motivated from the *WMAP* result (Spergel et al. 2003). CMB measurements probe large length-scale fluctuations and the constraint on the running spectral index is to some extent diluted by the other parameter uncertainties (especially the optical depth τ). In fact, strong constraints on the running of the spectral index can be obtained only by combining CMB, galaxy surveys and the $\text{Ly}\alpha$ forest. Weak lensing directly probes the relevant small length-scales, and is not susceptible to uncertainties due to biasing. The measured spectra however have undergone non-linear evolution, so an accurate model is needed to infer the shape of the linear spectrum.

To make forecasts for future lensing surveys, we follow the model in Spergel et al. (2003), where the linear mass power spectrum is expressed as

$$P_\delta(k) \propto \left(\frac{k}{k_0}\right)^{n+\alpha_s \ln(k/k_0)/2} T^2(k), \quad (39)$$

where $\alpha_s = dn/d \ln k$ and $k_0 = 0.05 \text{ Mpc}^{-1}$ and $T(k)$ is the transfer function. Fig. 10 shows the forecast constraints on w_0 , w_a and $dn/d \ln k$, for the two redshift bins. Here we considered eight parameters in the Fisher matrix analysis ($dn/d \ln k$, plus the seven parameters we have used so far), which enlarges the constraint ellipses in Fig. 6. It is clear that lensing tomography can put stringent constraints on the running spectral index: $\sigma(dn/d \ln k) = 0.0037 f_{\text{sky}}^{-1/2}$. This result can be compared with the constraint $\sigma(dn/d \ln k) = 0.004$ expected from the *Planck* mission (see table 2 in Eisenstein et al. 1999) and with the constraints expected from galaxy redshift surveys ($\sigma(dn/d \ln k) = 0.42$) and the $\text{Ly}\alpha$ forest ($\sigma(dn/d \ln k) = 0.04$ in Mandelbaum et al. 2003).² For this parameter the bispectrum is especially powerful, as evident from Fig. 10.

6 CONCLUSION AND DISCUSSION

We have used lensing tomography with the power spectrum and bispectrum as a probe of dark energy evolution and the mass power spectrum. The lensing bispectrum has different dependences on the lensing weight function and the growth rate of mass clustering from those of the power

² Note that the definition of k_0 in the model (39) differs in these papers, which affects the 1σ error.

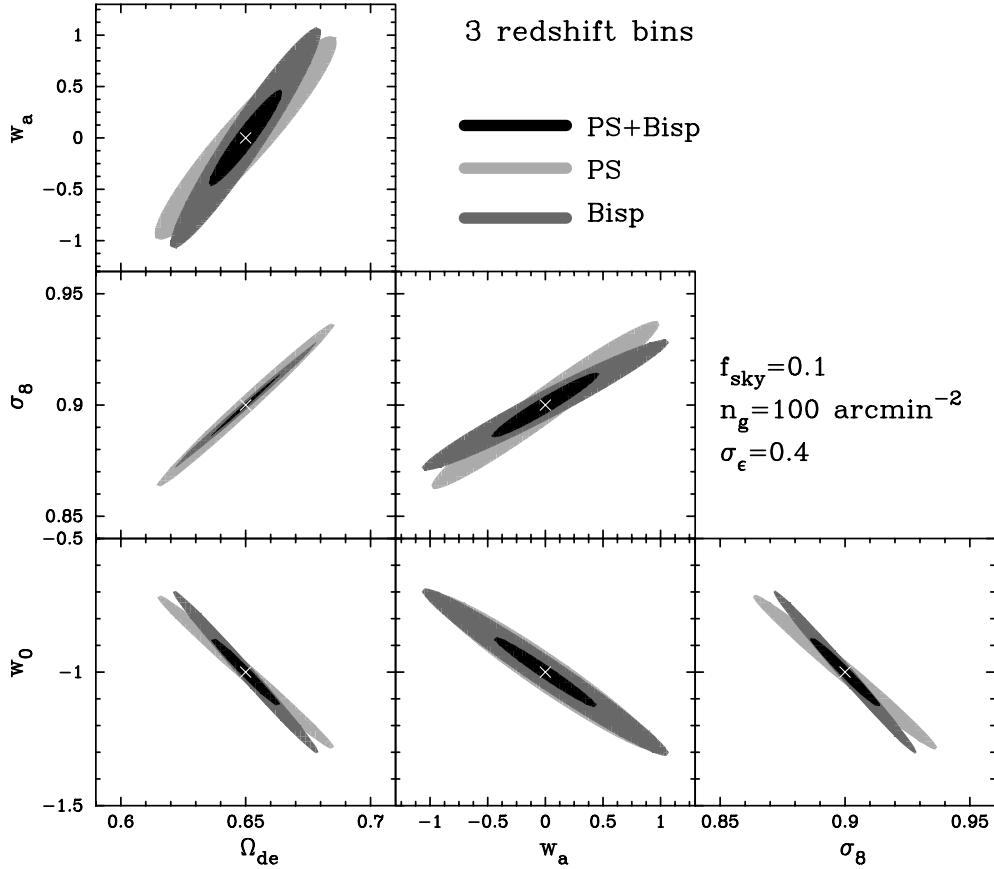


Figure 7. As in the previous figure, but for three redshift bins. In this case, we use six power spectra and 27 bispectra in the analysis. This figure is available in colour in the on-line version of the journal on *Synergy*.

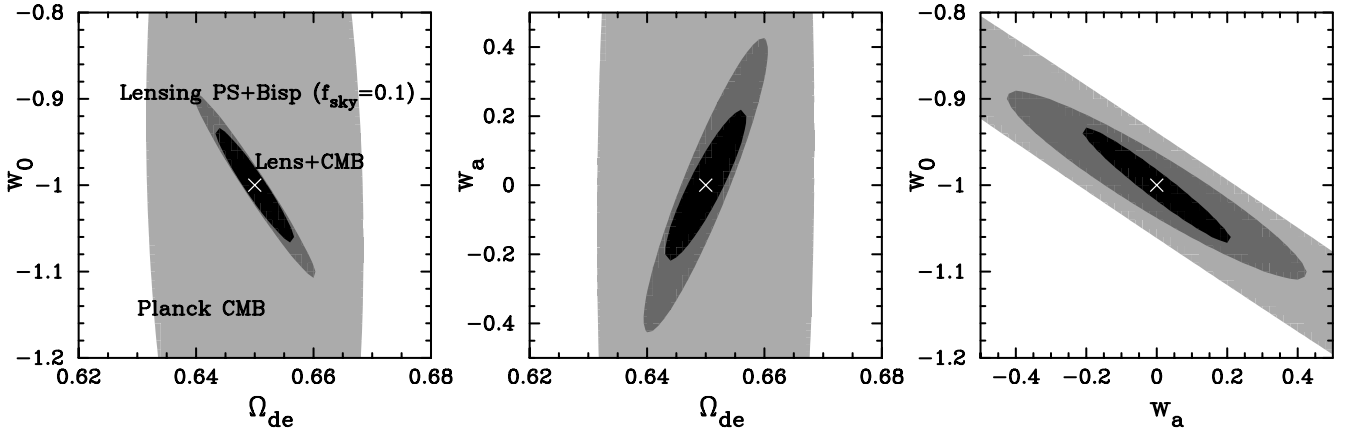


Figure 8. Error ellipses (68 per cent CL) for dark energy parameters (Ω_{de} , w_0 , w_a) when we use lensing tomography (PS + Bispectrum) with three redshift bins, CMB power spectra from the *Planck* experiment and combine the two. The constraints include marginalization over the other parameters, including the optical depth (see the text in more detail). This figure is available in colour in the on-line version of the journal on *Synergy*.

spectrum. Thus bispectrum tomography provides complementary constraints on cosmological parameters to power spectrum tomography. By using information from different triangle configurations and all cross-spectra in redshift bins we find that the bispectrum has roughly as much information as the power spectrum on parameters of interest (see Figs 6 and 7). Parameter accuracies are typically improved by a factor of 3 if both the power spectrum and bispectrum are used, compared to the standard approach of using just the power spectrum (see Table 1). Thus our study provides strong motivation for the use of the bispectrum from lensing surveys for parameter extraction.

Because lensing observables are significantly affected by non-linear gravitational clustering on angular scales below 1° , we used a non-linear model (see discussion below) to compute the lensing bispectrum and to estimate the precision on the parameters σ_8 , Ω_{de} , w_0 , w_a and $dn/d \ln k$. The constraints on the dark energy parameters are $\sigma(w_0) \sim 0.03 f_{\text{sky}}^{-1/2}$ and $\sigma(w_a) \sim 0.1 f_{\text{sky}}^{-1/2}$ – this sensitivity to the redshift evolution

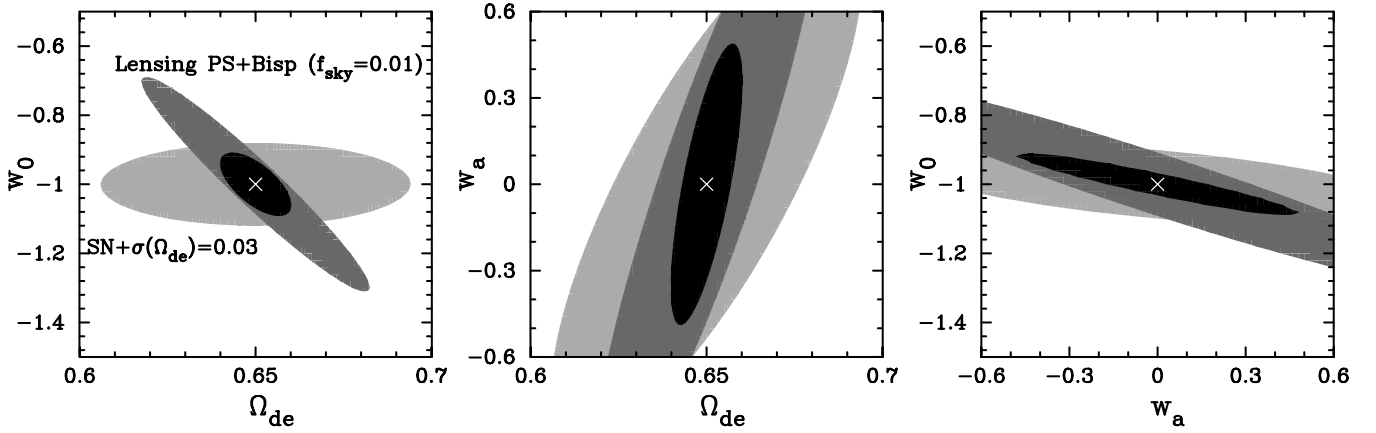


Figure 9. Parameter accuracy forecasts for the proposed *SNAP* survey of Type Ia supernovae and weak lensing, and the joint constraints from the two measurements. Note that the sky coverage $f_{\text{sky}} = 0.01$ is assumed for the lensing survey and we used the prior $\sigma(\Omega_{\text{de}}) = 0.03$ for the supernova constraint. This figure is available in colour in the on-line version of the journal on *Synergy*.

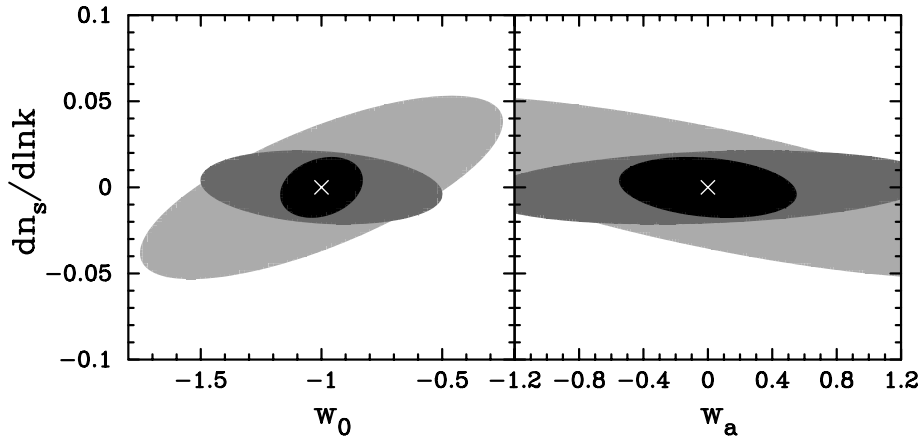


Figure 10. The constraint ellipses in the parameter space of w_0 , w_a and the running spectral index parameter $dn/d \ln k$. The Fisher analysis is as for Fig. 6. In total, eight parameters are considered to obtain the marginalized ellipses shown ($dn/d \ln k$, plus the seven parameters considered in the preceding analysis). This figure is available in colour in the on-line version of the journal on *Synergy*.

of the equation of state of dark energy is comparable to the best methods proposed for the coming decade. Moreover, external information on dark energy parameters such as provided by CMB and Type Ia supernova measurements can significantly improve the parameter accuracies as shown in Figs 8 and 9. In addition, lensing tomography can precisely probe the mass power spectrum: the constraint on the power spectrum amplitude is $\sigma(\sigma_8) \sim 4 \times 10^{-3} f_{\text{sky}}^{-1/2}$, and on the running spectral $\sigma(dn/d \ln k) \sim 4 \times 10^{-3} f_{\text{sky}}^{-1/2}$. Our analysis includes the full information at the two- and three-point level. Using three-point statistics such as the skewness, which contain no information on triangle configurations, weakens parameter constraints significantly.

Thus there is strong motivation to build an accurate model of lensing observables in the moderately non-linear regime. This should be feasible, as the physics involved in lensing is only gravity. It will also be necessary to calibrate the covariance of the bispectrum over relevant triangle configurations using a sufficient number of simulation realizations. Such an accurate model of the lensing bispectrum might modify the ellipse shapes in Fig. 6. Even so, we believe that the level of improvement from bispectrum tomography is likely to be correct, because the mass bispectrum we have employed should correctly estimate the amplitude, and therefore the S/N to within 10–20 per cent.

We also estimate how bispectrum tomography can put constraints on primordial non-Gaussianity. The most optimal constraint was estimated by requiring that the bispectrum due to primordial non-Gaussianity is detectable with $S/N \geq 1$. We neglected the bispectrum induced by gravitational non-Gaussianity, as it differs in its redshift evolution and configuration dependence. However, even with this assumption, the result in Fig. 4 is not very promising: the constraint on the primordial non-Gaussian model is not as stringent as that from the CMB bispectrum measurement (Komatsu et al. 2003), unless an almost all-sky lensing survey is available. It is worth exploring how the 3D mass reconstruction proposed by (Hu & Keeton 2002) could allow us to improve the lensing estimates.

We have concentrated on statistical measures of the convergence. However, the convergence field is not a direct observable, and reconstructing the convergence field from the measured ellipticities (shear) of galaxies is still challenging from survey data. Reconstruction techniques have been proposed for the power spectrum and the convergence field from realistic data (see Kaiser 1998; Hu & White 2001 for the 2D case and Taylor 2001 and Hu & Keeton 2002 for 3D mass reconstruction). It is of interest to develop an optimal method of extracting

the lensing bispectrum from the measured shear field. Alternatively, we can use measurements of the three-point correlation functions of the shear fields, which have been extensively studied recently by Schneider & Lombardi (2003), Zaldarriaga & Scoccimarro (2003) and TJ03a,c (see Bernardeau et al. 2002a; Pen et al. 2003; Jarvis, Bernstein & Jain 2004 for measurements). The shear three-point correlation functions carry full information on the convergence bispectrum (Schneider, Kilbinger & Lombardi 2004). Therefore, all the results derived in this paper are attainable using tomography of the two- and three-point functions of the shear fields.

There are other uncertainties we have ignored in this paper. We have assumed accurate photometric redshift measurements. For finite errors in the redshifts, we cannot take narrow redshift subdivisions of the galaxy distribution. This error would lead to additional statistical errors on measurements of the power spectrum and bispectrum and in turn on the cosmological parameters. Because we use only two or three redshift bins in our analysis, the demands on statistical errors are not very stringent. However, possible biases in the photometric redshifts must be carefully examined, because the redshift evolution of dark energy leads to only a small effect on the lensing observables, as discussed in Bernstein & Jain (2004).

We have also ignored the B -mode contamination to the lensing observables, though it is seen in current measurements (e.g. Jarvis et al. 2003). The main source is likely to be observational systematics which are not eliminated in the point spread function (PSF) correction. For a shallow survey, the intrinsic ellipticity alignments could also provide significant contribution to the B -mode on small angular scales. Another useful application of photometric redshift information is that it allows us to remove intrinsic alignment contaminations by excluding close pairs of galaxies in the same redshift bin (Heymans & Heavens 2003; King & Schneider 2003). Thus the cross-power spectrum calculated from different redshift bins is not affected by the intrinsic alignment. Hence, lensing tomography that uses the cross-power spectra and bispectra is robust to systematics (Takada & White 2004). The degradation in parameter accuracies is likely to be small, because the cross-power spectrum carries comparable lensing signal to the auto-spectrum (see Fig. 2 and Takada & White 2004).

ACKNOWLEDGMENTS

We thank G. Bernstein, D. Dolney, M. Jarvis, E. Komatsu, W. Hu, L. King, E. Linder, S. Majumdar, A. Refregier, P. Schneider, R. Scoccimarro and M. White for useful discussions. We also thank U. Seljak and M. Zaldarriaga for making updated versions of CMBFAST publicly available. We acknowledge the hospitality of the Aspen Center for Physics, where this work was begun. This work is supported by NASA grants NAG5-10923, NAG5-10924 and a Keck foundation grant.

REFERENCES

- Abazajian K. N., Dodelson S., 2003, *Phys. Rev. Lett.*, 91, 041301
 Bardeen J. M., Bond J. R., Kaiser N., Szalay A. S., 1986, *ApJ*, 304, 15 (BBKS)
 Bartelmann M., Schneider P., 2001, *Phys. Rep.*, 340, 291
 Benabed K., Bernardeau F., 2001, *Phys. Rev. D.*, 64, 3501
 Benabed K., Van Waerbeke L., 2004, *Phys. Rev. D*, submitted (astro-ph/0306033)
 Bernardeau F., Mellier Y., Van Waerbeke L., 2002a, *A&A*, 389, L28
 Bernardeau F., Colombi S., Gaztañaga E., Scoccimarro R., 2002b, *Phys. Rep.*, 367, 1
 Bernstein G., Jain B., 2004, *ApJ*, in press (astro-ph/0309332)
 Blandford R. D., Saust A. B., Brainerd T. G., Villumsen J. V., 1991, *MNRAS*, 251, 600
 Boughn S. P., Crittenden R. G., 2003, preprint (astro-ph/0305001)
 Caldwell R. R., Dave R., Steinhardt P. J., 1998, *Phys. Rev. Lett.*, 80, 1582
 Chiba T., Nakamura T., 2000, *Phys. Rev. D.*, 62, 121301
 Cooray A., Hu W., 2001a, *ApJ*, 548, 7
 Cooray A., Hu W., 2001b, *ApJ*, 554, 56
 Cooray A., Sheth R., 2002, *Phys. Rep.*, 372, 1
 Dvali G., Gruzinov A., Zaldarriaga M., 2003, preprint (astro-ph/0305548)
 Eisenstein D. J., Hu W., Tegmark M., 1999, *ApJ*, 518, 2
 Falk T., Rangarajan R., Srednicki M., 1993, *ApJ*, 403, L1
 Frieman J., Huterer D., Linder E., Turner M. S., 2003, *Phys. Rev. D.*, 67, 083505
 Futamase Y., Yoshida S., 2001, *Prog. Thor. Phys.*, 105, 887
 Gangui A., Luchin F., Matarrese S., Mollerach S., 1994, *ApJ*, 430, 447
 Hamana T. et al., 2003, *ApJ*, 597, 98
 Heavens A., 2003, *MNRAS*, 343, 1237
 Heymans C., Heavens A., 2003, *MNRAS*, 339, 711
 Hu W., 1999, *ApJ*, 522, L21
 Hu W., 2000, *Phys. Rev. D.*, 62, 043007
 Hu W., 2002a, *Phys. Rev. D.*, 65, 023003
 Hu W., 2002b, *Phys. Rev. D.*, 66, 083515
 Hu W., Keeton C., 2002, *Phys. Rev. D.*, 66, 3506
 Hu W., White M., 2001, *ApJ*, 554, 67
 Hui L., 1999, *ApJ*, 519, L9
 Huterer D., 2002, *Phys. Rev. D.*, 65, 3001
 Huterer D., Turner M., 2001, *Phys. Rev. D.*, 64, 123527
 Jain B., Seljak U., 1997, *ApJ*, 484, 560
 Jain B., Taylor A., 2003, *Phys. Rev. Lett.*, 91, 141302

- Jarvis M., Bernstein G. M., Fischer P., Smith D., Jain B., Tyson J. A., Wittman D., 2003, *AJ*, 125, 1014
Jarvis M., Bernstein G., Jain, 2004, *MNRAS*, submitted (astro-ph/0307393)
Jenkins A., Frenk C. S., White S. D. M., Colberg J. M., Cole S., Evrard A. E., Couchman H. M. P., Yoshida N., 2001, *MNRAS*, 321, 372
Kaiser N., 1992, *ApJ*, 388, 272
Kaiser N., 1998, *ApJ*, 498, 26
King L. J., Schneider P., 2003, *A&A*, 398, 23
Komatsu E., 2001, PhD thesis, Univ. Tohoku (astro-ph/0206039)
Komatsu E. et al., 2003, *ApJS*, 148, 119
Linder E., 2003, *Phys. Rev. Lett.*, 90, 091301
Linder E., Jenkins A., 2003, *MNRAS*, 346, 573
Luo X., 1994, *ApJ*, 427, L71
Ma C.-P., Caldwell R. R., Bode P., Wang L., 1999, *ApJ*, 521, L1
Mandelbaum R., McDonald P., Seljak U., Cen R., 2003, *MNRAS*, 344, 776
Massey R. et al., 2004, *ApJ*, submitted (astro-ph/0304418)
Matarrese S., Verde L., Jimenez R., 2000, *ApJ*, 541, 10
Matsubara T., Szalay A. S., 2002, *ApJ*, 574, 1
Mellier Y., 1999, *ARA&A*, 37, 127
Miralda-Escude J., 1991, *ApJ*, 380, 1
Nolta M. R. et al., 2004, *ApJ*, submitted (astro-ph/0305097)
Padmanabhan T., 2003, *Phys. Rep.*, 380, 235
Peebles P. J. E., Ratra B., 2003, *Rev. Mod. Phys.*, 75, 559
Pen U. L., Zhang T., Van Waerbeke L., Mellier Y., Zhang P., Dubinski J., 2003, *ApJ*, 592, 664
Perlmutter S. et al., 1999a, *ApJ*, 517, 565
Perlmutter S., Turner M. S., White M., 1999b, *Phys. Rev. Lett.*, 83, 670
Refregier A. et al., 2004, *ApJ*, submitted (astro-ph/0304419)
Riess A. G. et al., 1998, *AJ*, 116, 1009
Schneider P., 2003, *A&A*, 408, 829
Schneider P., Lombardi M., 2003, *A&A*, 397, 809
Schneider P., Kilbinger M., Lombardi M., 2004, *AA*, submitted (astro-ph/0308328)
Scoccimarro R., Couchman H. M. R., 2001, *MNRAS*, 325, 1312
Scoccimarro R., Frieman J., 1999, *ApJ*, 520, 35
Scoccimarro R., Zaldarriaga M., Hui L., 1999, *ApJ*, 527, 1
Scranton R. et al., 2004, *Phys. Rev. Lett.*, submitted (astro-ph/0307335)
Seljak U., Zaldarriaga M., 1996, *ApJ*, 469, 437
Simon P., King L. J., Schneider P., 2004, *A&A*, submitted (astro-ph/0309032)
Smith R. E. et al., 2003, *MNRAS*, 341, 1311 (Smith03)
Spergel D. N. et al., 2003, *ApJ Suppl.*, 148, 175
Sugiyama N., 1995, *ApJS*, 100, 281
Takada M., Hamana T., 2003, *MNRAS*, 346, 949
Takada M., Jain B., 2002, *MNRAS*, 337, 875 (TJ02)
Takada M., Jain B., 2003a, *ApJ*, 583, L49 (TJ03a)
Takada M., Jain B., 2003b, *MNRAS*, 340, 580 (TJ03b)
Takada M., Jain B., 2003, *MNRAS*, 344, 857 (TJ03c)
Takada M., White M., 2004, *ApJL*, in press (astro-ph/0311104)
Taylor A. N., 2001, pre-print (astro-ph/0111605)
Tegmark M., 2002, *Phys. Rev. D.*, 66, 103507
Tegmark M., Taylor A., Heavens A., 1997, *ApJ*, 480, 22
Turner M. S., White M., 1997, *Phys. Rev. D.*, 56, R4439
Verde L., Wang L., Heavens A. F., Kamionkowski M., 2000, *MNRAS*, 313, 141
Van Waerbeke L., Mellier Y., 2003, preprint (astro-ph/0305089)
Wang L., Kamionkowski M., 2000, *Phys. Rev. D.*, 61, 063504
Wang L., Steinhardt P. J., 1998, 508, 483
Weinberg N. N., Kamionkowski M., 2003, *MNRAS*, 341, 251
Weinberg S., 1989, *Mod. Rev. Phys.*, 61, 1
White M., Hu W., 2000, *ApJ*, 537, 1
Zaldarriaga M., 2003, preprint (astro-ph/0306006)
Zaldarriaga M., Scoccimarro R., 2003, *ApJ*, 590, 1

APPENDIX A: APPROXIMATION FOR WIGNER-3j EVALUATION

The expression for the bispectrum of the convergence field involves the Wigner-3j symbol, which has a closed algebraic form (e.g. Hu 2000):

$$\begin{pmatrix} l_1 & l_2 & l_3 \\ 0 & 0 & 0 \end{pmatrix} = (-1)^{L/2} \frac{(L/2)!}{(L/2 - l_1)! (L/2 - l_2)! (L/2 - l_3)!} \left[\frac{(L - 2l_1)! (L - 2l_2)! (L - 2l_3)!}{(L + 1)!} \right]^{1/2}, \quad (\text{A1})$$

for even $L = l_1 + l_2 + l_3$ and zero for odd L .

Rather than using the exact equation, we employ an approximation of the Wigner-3j symbol evaluation, as the direct numerical calculation encounters a divergence problem in the factorial as $l!$ for large l . For this purpose, we use the Stirling approximation: $n! = \Gamma(n + 1)$ and

$$\Gamma(x) \sim (2\pi)^{1/2} e^{-x} x^{x-1/2}, \quad \text{for large } x. \quad (\text{A2})$$

This approximation is quite good, leading to errors less than 0.2 per cent for angular scales $l \geq 50$ of our interest. Using this approximation, the expression (A1) of the Wigner-3j symbol is rewritten as

$$\begin{aligned} \begin{pmatrix} l_1 & l_2 & l_3 \\ 0 & 0 & 0 \end{pmatrix} &\approx (-1)^{L/2} (2\pi)^{-1/2} e^{3/2} 2^{1/4} (L+2)^{-1/4} \left(\frac{L/2 - l_1 + 1/2}{L/2 - l_1 + 1} \right)^{L/2 - l_1 + 1/4} \left(\frac{L/2 - l_1 + 1/2}{L/2 - l_1 + 1} \right)^{L/2 - l_2 + 1/4} \\ &\times \left(\frac{L/2 - l_1 + 1/2}{L/2 - l_1 + 1} \right)^{L/2 - l_3 + 1/4} \frac{1}{(L/2 - l_1 + 1)^{1/4} (L/2 - l_2 + 1)^{1/4} (L/2 - l_3 + 1)^{1/4}}. \end{aligned} \quad (\text{A3})$$

This paper has been typeset from a $\text{\TeX}/\text{\LaTeX}$ file prepared by the author.